ACCSCIENCE PUBLISHING

International Journal of Bioprinting

RESEARCH ARTICLE

Innovative design and compression performance of selective laser melting-printed tantalum artificial vertebral bodies

Yutao Zhang[1], Wurikaixi Aiyiti[2*], Jintao Li[1,2], Yong Huang[1,3], and Xiaohong Dong[1]

[1]Xinjiang Coal Mine Electromechanical Engineering Technology Research Center, School of Electromechanical Engineering, Xinjiang Institute of Engineering, Urumqi, Xinjiang, China

[2] Xinjiang Additive Remanufacturing Technology Key Laboratory, School of Mechanical Engineering, Xinjiang University, Urumqi, Xinjiang, China

[3]Key Laboratory of Intelligent Manufacturing Technology for Building Steel Structures of Xinjiang Production and Construction Corps, Urumqi, Xinjiang, China

Abstract

Tantalum (Ta) holds considerable potential for clinical applications in artificial vertebral bodies (AVBs) owing to its excellent biocompatibility. A novel Ta AVB structure was engineered by combining thin-walled structure topology optimization with lattice structure filling design methods. Three types of Ta AVBs—designated as AVB-1, AVB-2, and AVB-3—were fabricated using selective laser melting. The influence of sidewall curvature on the mechanical properties and deformation behavior of AVBs was investigated through compression tests and finite element analysis. The elastic modulus and yield strength of the Ta lattice structures ranged from 1.75 to 3.21 GPa and 31 to 65 MPa, respectively. Incorporating topologically thin walls enhanced the elastic modulus and yield strength by factors of 2.26–3.77 and 3–3.62, respectively. A decrease in sidewall curvature was associated with an increase in both elastic modulus and yield strength of the AVBs. Specifically, as the sidewall curvature decreased from 0.027 to 0 mm^{-1}, the elastic modulus and yield strength increased by factors of 2.76 and 2.19, respectively. The yield strengths of the AVBs were comparable to those of human cortical bone. Among the three designs, AVB-2 exhibited the highest yield-strength-to-elastic-modulus ratio (0.029), compared to AVB-1 and AVB-3 (0.024 and 0.019, respectively), suggesting that the optimal sidewall curvature is 0.014 mm^{-1}. AVB-2 effectively mitigated the stress shielding effect while maximizing the load-bearing capacity, indicating its significant potential for clinical applications.

Keywords: Tantalum; Selective laser melting; Artificial vertebral body; Lattice structure; Topology optimization

***Corresponding author:**
Wurikaixi Aiyiti
(wurikaixi@xju.edu.cn)

Citation: Zhang Y, Aiyiti W, Li J, Huang Y, Dong X. Innovative design and compression performance of selective laser melting-printed tantalum artificial vertebral bodies. *Int J Bioprint*. 2025;11(4):165-188. doi: 10.36922/IJB025150133

Received: April 11, 2025
Revised: May 5, 2025
Accepted: May 16, 2025
Published Online: May 16, 2025

1. Introduction

Total *en bloc* spondylectomy is an effective treatment for spinal tumors and tuberculosis. This procedure involves the complete removal of the diseased vertebral body and the

restoration of the spinal stability through the implantation of an artificial vertebral body (AVB).[1] The AVB should possess adequate load-bearing capacity and good osseointegration, with an elastic modulus that closely matches that of human bone to avoid stress shielding.[2] Research aimed at enhancing the performance of AVBs has focused on innovations in materials and optimized structural designs.[3–7]

Current studies have shown that titanium (Ti) and its alloys,[8] polyetheretherketone (PEEK),[9,10] and hydroxyapatite (HA)[11] are potential materials for use in AVBs. Although PEEK has an elastic modulus close to that of human bone, it suffers from limited load-bearing capacity and poor bioactivity, factors that have become bottlenecks in its application.[10] In contrast, HA exhibits excellent biocompatibility, but its low fracture toughness limits its use in this field.[12] To address the limitations associated with the performance of single materials, researchers have attempted to develop composites based on polymers or HA.[13–15]

Owing to their excellent mechanical stability and bioactivity, Ti and its alloys are widely used in bone implants such as hip and knee replacements, dental implants, spinal implants, and cranial defect repairs.[8,16] Compared to PEEK and HA, Ti alloys exhibit superior load-bearing capacities, making them more suitable for applications in load-bearing parts of the human body.[17,18] As a result, Ti alloys have become mainstream materials for the clinical application of AVBs. Furthermore, traditional Ti alloy cages (Ti cages) have been widely adopted for the clinical treatment of spinal diseases.[19–21]

Tantalum (Ta), a transition metal, demonstrates notable physical properties, including a high density (16.68 g/cm^3) and a high melting point (2996 °C). In addition to its reliable mechanical properties, Ta demonstrates superior bioactivity, corrosion resistance, and fracture toughness compared with Ti alloys,[22–24] thereby significantly enhancing the osseointegration of bone implants. Tantalum pentoxide (Ta_2O_5) films, which form readily on the surface of Ta metal, offer excellent corrosion resistance and osteoinductive function.[25] Therefore, Ta has great potential for applications in AVBs.[26] Unfortunately, the elastic moduli of solid Ta (186 GPa) and Ti (110 GPa) considerably exceed that of human bone (0.022–21 GPa),[27] leading to stress shielding of the vertebrae and poor integration of the AVB with the surrounding bone tissue.[28] By utilizing topology optimization and lattice design, the elastic modulus of the Ta AVB can be substantially decreased, enabling better matching with that of human bone.[29]

The lattice structure was fabricated by a periodic arrangement of multiple identical unit cells. Thanks to their superior specific strength and specific stiffness relative to solid materials, lattice structures have garnered significant attention for applications in lightweight design, energy absorption, and biomedicine.[30,31] Moreover, the interconnected open pores within the lattice structure facilitate the ingrowth of cells and blood vessels, thereby significantly improving the osseointegration of bone implants.[32–36] Therefore, incorporating lattice structures into the Ta AVB substantially reduces its elastic modulus and improves its biocompatibility. Chen et al.[37] designed a Ta density-gradient lattice structure. The elastic moduli of these lattice structures ranged from 0.22 to 0.89 GPa, which is similar to that of human cancellous bone. Song and colleagues[38] proposed gyroid porous Ta structures with radially graded porosity. Compression tests showed that the porous Ta structures had a minimum elastic modulus of 0.6 GPa. Ni et al.[39] compared the fatigue performance of a triple periodic minimal surface (TPMS) and rhombic dodecahedron Ta lattice structures. The TPMS structure exhibited higher fatigue resistance than the rhombic dodecahedron and has the potential for use in load-bearing bone implants.

Topology optimization design identifies the optimal force transfer paths and structural morphology by adjusting the distribution of materials within the design domain. This approach reduces material usage while improving the structural mechanical properties.[40] When applied to the structural optimization of bone implants, this design methodology enables regulation of overall stiffness,[41] achieving an optimal balance between maximizing load-carrying capacity and minimizing stress shielding by tailoring the mechanical properties of the implant.[42,43] Kök and colleagues[42] applied topology optimization to the internal structure of dental implants and reported a 30% reduction in stress shielding compared to standard implants. Peng et al.[44] implemented topology optimization in the fixation system of a mandibular implant, resulting in improved mechanical stability. In their work on interbody fusion cages, Smit and colleagues[45] incorporated the structural response of adjacent bone into the topology optimization process, significantly reducing the risk of cage subsidence.

Owing to significant advancements in metal additive manufacturing processes, the preparation of customized bone implants featuring complex structures has become feasible. Selective laser melting (SLM), a representative metal additive manufacturing technology, is characterized by high resolution and high energy input, enabled by precise laser control. This capability makes SLM particularly suitable for producing fine and complex structures, such as lattices and topological configurations, even with high-melting-point materials like Ta.[46,47] Wang

et al.[48] fabricated trabecular Ta specimens using laser powder bed fusion (LPBF) and investigated the effects of annealing temperature and oxygen content on their mechanical properties. Qin and colleagues[49] performed hot isostatic pressing to LPBF-printed TPMS porous Ta, significantly improving its compressive strength without compromising plasticity. Functional gradient Ta lattice structures developed by Chen et al.[37] using LPBF exhibited excellent manufacturability, with a porosity deviation of less than 5.13%.

Extensive research has been conducted on the optimal design of spinal implant structures. However, there remains a notable lack of studies focused on optimizing the overall architecture of AVBs to minimize stress shielding while maximizing load-bearing capacity. Moreover, investigations into the mechanical properties of SLM-fabricated Ta AVBs are limited, especially in comparison with polymer- and Ti alloy-based spinal implants.

In this study, novel Ta AVBs were developed by integrating topology optimization and lattice structure design methods and fabricated using SLM. The influence of sidewall curvature on the mechanical properties and deformation behavior of these AVBs was investigated through compression tests and finite element analysis. The objective was to optimize AVB's overall structure to effectively reduce the stress shielding effect, enhance load-bearing functionality, and align its mechanical properties with those of the human cortical bone. This study aimed to develop a novel Ta AVB with the potential to enhance osseointegration and mitigate the risk of bone resorption in cervical fusion segments and degenerative diseases in the adjacent segments. The logical flow of the introduction section of the article is shown in Figure 1.

2. Materials and methods

2.1. Design method

The Ta AVB was designed to imitate human vertebrae and is composed of a thin-walled and lattice structure, as shown in Figure 2. The height of the AVB was set at 24 mm, and the end face was designed to be elliptical, with a long diameter of 16 mm and a short diameter of 12.6 mm. The thin-walled structure functioned similarly to the cortical bone of the human vertebrae and was used to

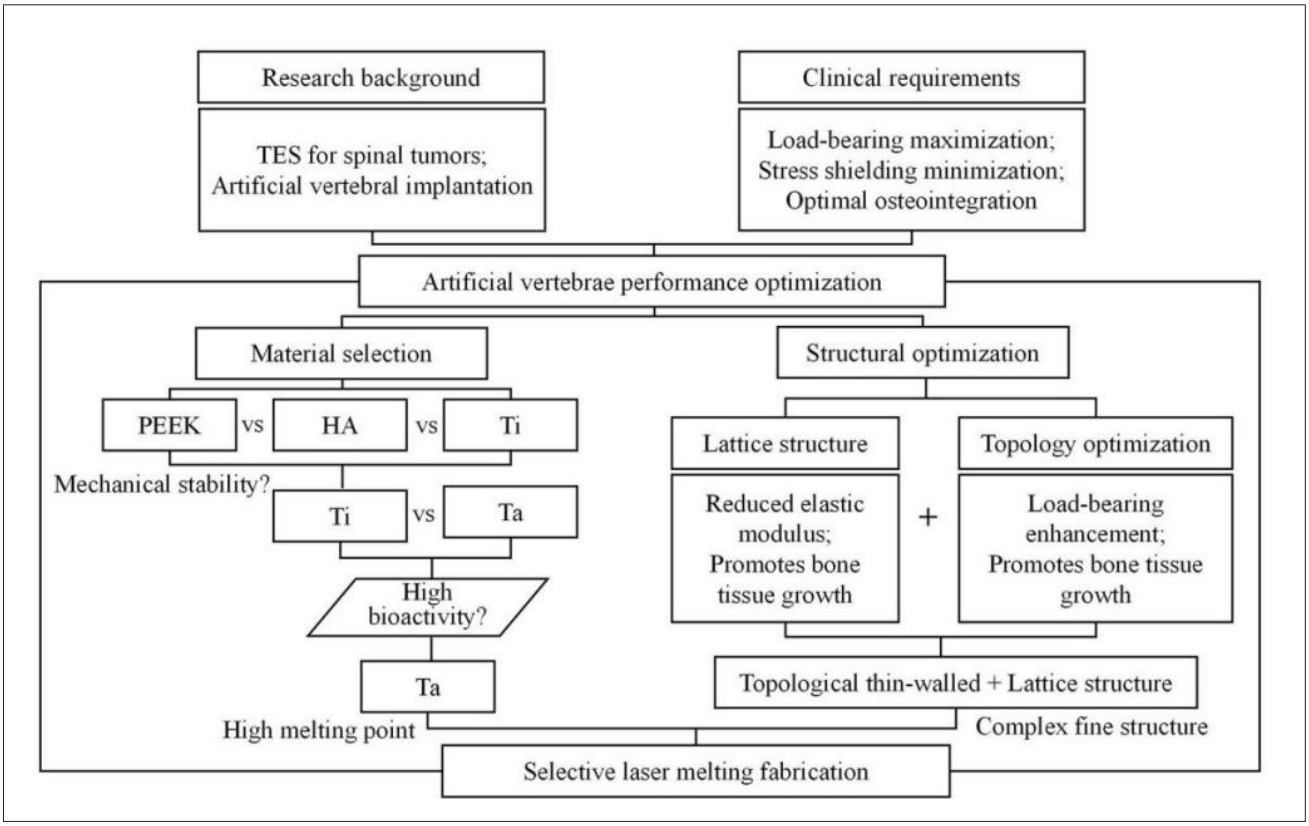

Figure 1. Logical flow of **Introduction** section. Abbreviations: HA: Hydroxyapatite; PEEK: Polyetheretherketone; Ta: Tantalum; TES: Total *en bloc* spondylectomy; Ti: Titanium.

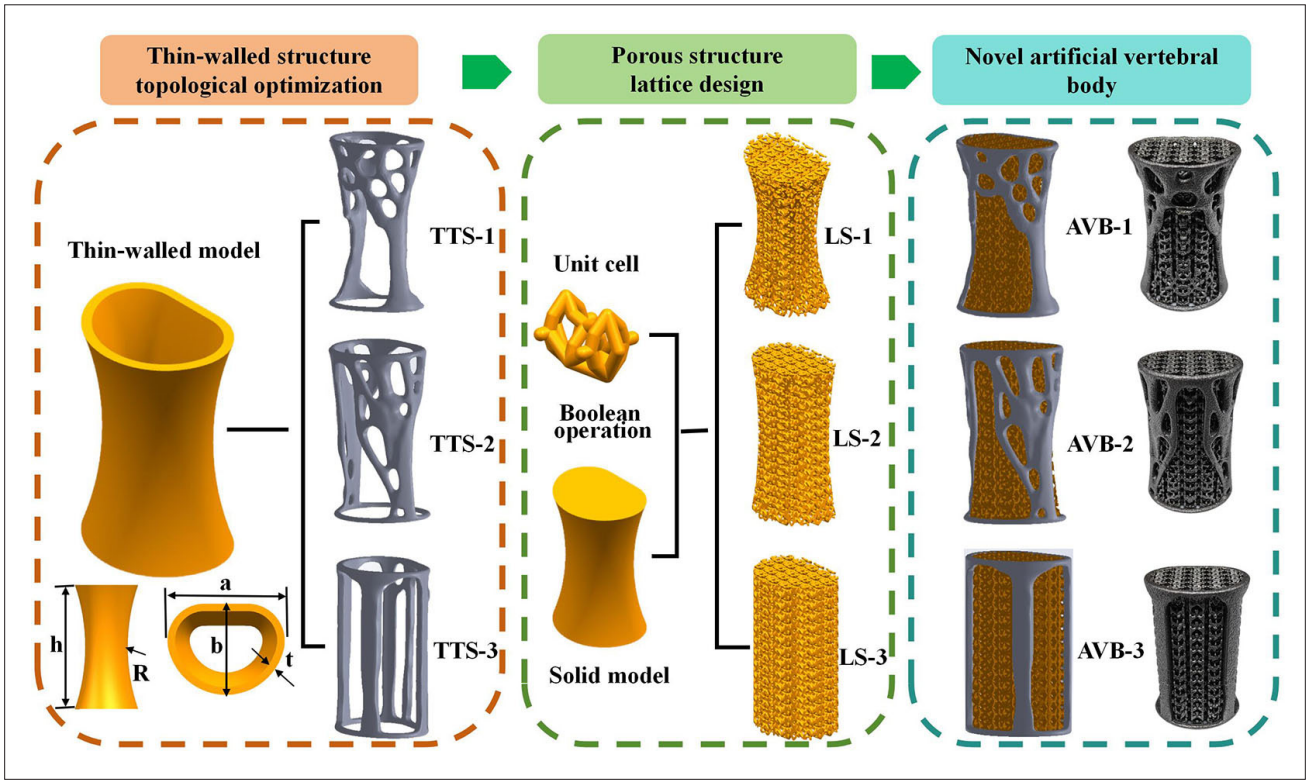

Figure 2. Schematic representation of thin-walled structure topology optimization, lattice structure filling, and artificial vertebral body model design. Abbreviations: a: Long diameter; AVB: Artificial vertebral body; b: Short diameter; h: Height; LS: Lattice structure; R: Radius of curvature; t: Thickness; TTS: Topological thin-walled structure.

enhance load-bearing capacity. Thin walls were designed with pores to provide channels for cell migration, blood vessel growth, and bone tissue formation. To maximize the load-bearing performance of thin walls with pores, a topology optimization design of the thin-walled structure was carried out in this study.

Common methods used for topology optimization of continuum structures include homogenization, variable density, evolutionary structural optimization, level set, and independent continuous mapping (ICM) methods. The variable density method considers continuum structures to consist of elements with variable densities. The element densities vary in the range [0, 1], which transforms the material distribution into a [0, 1] integer programming. An element density of zero indicates that the material at that location can be discarded, while a density of one indicates that the material should be retained. Intermediate densities are brought closer to zero or one by introducing a penalty factor. The relationship between the element density and elastic modulus is defined as follows:

$$E_i = E_{min} + f(\rho_i) \times (E_0 - E_{min}) \quad \text{(I)}$$

where E_i is the elastic modulus of the i-th element, E_{min} is the minimum elastic modulus, $f(\rho_i)$ is the penalty function, and E_0 is the elastic modulus of the initial design domain.

A solid isotropic material with penalization (SIMP) model was used to optimize the load transfer path and material distribution in the thin-walled structures. The penalty function for the SIMP interpolation model is expressed as:

$$f(\rho_i) = \rho_i^P \quad \text{(II)}$$

where ρ_i is the density of the i-th element and P is the penalty factor.

The optimization aims to minimize structural compliance under specific boundary conditions and volume constraints. The mathematical model for topology optimization is as follows[50]:

$$\begin{cases} Find\ \rho = (\rho_1, \rho_2, ..., \rho_n); \\ min C(\rho) = \frac{1}{2} U^T K U = \frac{1}{2} \sum_{i=1}^{n} u_i^T k_0 (\rho_i)^p E_s u_i; \\ s.t.\ \frac{V_\rho}{V_0} \le f; \\ 0 < \rho_{min} < \rho_i \le 1 \end{cases} \quad \text{(III)}$$

where ρ is the density of the element, C is compliance, U is the global displacement vector, K is the global stiffness matrix, n is the number of elements, u_i is the element displacement vector, k_0 is the element stiffness matrix for unit Young's modulus, E_s is the stiffness of the material, p is the penalization factor, V_ρ and V_0 are the material volume and the design domain volume, respectively, f is the prescribed volume fraction, and ρ_{min} is the minimum element density.

Altair OptiStruct™ software (Altair Engineering Inc., USA) was used for the topology optimization design of the thin-walled model. The mesh type was tetrahedral, and the mesh size was set to 0.5 mm. The material properties of Ta were assigned to the mesh elements, with an elastic modulus of 186 GPa, a Poisson's ratio of 0.35, and a density of 16.6 g/cm^3. The boundary conditions were defined such that the bottom surface of the thin-walled model was fully constrained and a pressure of 2 MPa was applied to the top surface. The topology optimization parameters were set to a minimum size of 0.5 and a maximum size of 1. The prescribed volume fraction, penalization factor, and minimum element density were set to 0.3, 3, and 0.01, respectively.

The key design parameters affecting the mechanical properties of thin-walled structures are wall thickness and sidewall curvature. While it is evident that increasing wall thickness enhances load-bearing capacity, sidewall curvature has more complex effects on the mechanical properties of both the thin-walled structure and its internal lattice. Furthermore, an excessively thick outer wall can hinder the inward growth of bone tissue and reduce the fusion rate of the AVBs. This study focused on evaluating the effect of sidewall curvature on the mechanical properties of AVBs with a wall thickness of 1 mm. As shown in Figure 2, three topological thin-walled structures, named TTS-1, TTS-2, and TTS-3, were designed with sidewall curvatures of 0.027, 0.014, and 0 mm^{-1}, respectively.

The interior of the topological thin-walled structure imitated the cancellous bone and was designed as an interconnected porous architecture to enhance osseointegration and promote nutrient transport. The lattice structure was constructed through a periodic arrangement of identical unit cells. A strut is the basic component of a strut-based unit cell and plays a crucial role in determining its mechanical properties. The elastic moduli of unit cells with straight struts can be obtained using the Euler–Bernoulli and Timoshenko beam theories.[51] Based on the Euler–Bernoulli beam theory, the strut displacement along the z-axis under compression is given by:

$$\delta_z = \frac{Fl^3 \cos^2\theta}{12 E_s I} + \frac{Fl \sin^2\theta}{E_s A} \quad \text{(IV)}$$

where F is the force on the strut, θ is the angle between the strut and the horizontal axis, A is the cross-sectional area of the strut, and I is the moment of inertia, defined as $I = \pi d^4/64$.

In addition to the strut deformation caused by axial loads and bending moments, the Timoshenko beam theory also considers the strut shear deformation. The strut displacement along the z-axis can be calculated as follows:

$$\delta_z = \frac{Fl^3 \cos^2\theta}{12 E_s I} + \frac{Fl \sin^2\theta}{E_s A} + \frac{Fl \cos^2\theta}{\kappa A G_s} \quad \text{(V)}$$

where κ is the shear coefficient factor, and G_s is the shear modulus of the parent material.

The displacement of the unit cell ($\delta_{UC,Z}$) can be obtained by accumulating strut displacements. Therefore, the strain in the unit cell can be expressed as follows:

$$\varepsilon_{UC,Z} = \frac{\delta_{UC,Z}}{h} \quad \text{(VI)}$$

where h is the height of the unit cell.

According to Hooke's law, the elastic modulus of a unit cell can be calculated as follows:

$$E_{UC,Z} = \frac{\sigma_{UC,Z}}{\varepsilon_{UC,Z}} \quad \text{(VII)}$$

where $\sigma_{UC,Z}$ is the stress of the unit cell along the z-axis.

According to the elastic–plastic cellular solid model proposed by Gibson and Ashby,[52] the plastic collapse stress of the lattice structure under compression can be calculated as:

$$\frac{\sigma_{pl}^{*}}{\sigma_{ys}} = \left(\frac{d}{l}\right)^{2} \quad \frac{1}{2cos^{2}\theta} \tag{VIII}$$

where σ_{ys} is the yield strength of the parent material.

Overall, the design parameters of the struts, such as the ratio of strut diameter to length (d/l), the inclination angle of the strut (θ), and the number of struts (s), have significant effects on the elastic modulus and yield strength of the lattice structures. In our previous study, compared to the conventional body-centered cubic lattice structure, the imitation saddle surface (ISS) featured more slightly angled inclined struts, a greater number of struts and nodes, and a higher strut diameter-to-length ratio. According to our previous results,[53] the ISS lattice structure exhibited a higher yield-stress-to-elastic-modulus ratio than the body-centered cubic lattice, effectively reducing the risk of stress shielding. Therefore, the ISS lattice structure was selected to fill the interior of the AVB.

Three lattice structures, named LS-1, LS-2, and LS-3, were generated through Boolean operations. Their sidewall curvatures were 0.027, 0.014, and 0 mm^{-1}, respectively. AVBs with the same corresponding sidewall curvatures named AVB-1, AVB-2, and AVB-3 were obtained by assembling topological thin-walled structures with lattice structures, as shown in Figure 2. Due to the small overall size of the AVB, a large sidewall curvature resulted in too few unit cells in the central region. Therefore, the maximum sidewall curvature was set at 0.027 mm^{-1} to ensure the stability of the lattice structure during compression.

Previous studies have indicated that bone implants with porosities between 0.6 and 0.8 are favorable for cell and bone tissue growth.[32,33,54] The porosity of the lattice structures (LS-1, LS-2, and LS-3) and the AVBs (AVB-1, AVB-2, and AVB-3) were designed to be 74% and 70%, respectively. The design and actual parameters of the Ta AVB and lattice structure specimens are presented in Table 1.

2.2. Specimen fabrication

Spherical pure Ta powder was used to fabricate the lattice structure and AVB specimens. As shown in Figure 3, the powder particle size distribution was D10 = 20.19 μm, D50 = 33.13 μm, and D90 = 52.37 μm. The chemical composition of the powder is listed in Table 2.

An SLM metal three-dimensional 3D printer (DiMetal-100 Pro; LASERADD, China) was employed to fabricate the Ta lattice structure and AVB specimens. The SLM printing parameters are provided in Table 3. Due to the small strut diameter (0.34 mm) and wall thickness (1 mm), the layer thickness was set to 0.03 mm to ensure high molding precision. The optimal process parameters of 350 W laser power, 650 mm/s scanning speed, and 0.08 mm hatch distance significantly improved the stability and fluidity of the Ta molten pool, reduced the number of defects, and resulted in Ta specimens with densities greater than 99.9%. An interlayer rotation angle of 67° was used to reduce anisotropy. The specimens were fabricated in a closed chamber under high-purity argon gas (99.9999%) to prevent oxidation. Post-processing included sandblasting and ultrasonic cleaning to remove residual powder particles from the printed Ta AVB specimens.

2.3. Morphological characterization

The dry weighing method was adopted to measure the porosity of the specimens, as follows:

$$p = 1 - \frac{m_d}{\rho_t V_a} \tag{IX}$$

where m_d is the mass of the specimen, ρ_t is the theoretical density of Ta, and V_a is the volume of the specimen.

The surface morphology and feature size of the specimens were measured using an ultra-depth microscope (VHX-6000; KEYENCE, Japan). As shown in Table 1, the porosities of the AVB-1, AVB-2, and AVB-3 specimens

Table 1. Design and actual values of selective laser melting-tantalum AVB and LS

Specimens	Porosity (%)		Thin-walled thickness (mm)		Lattice structure diameter (mm)	
	Design	Actual	Design	Actual	Design	Actual
AVB-1	70	71	1	0.98	0.34	0.35
AVB-2	70	69	1	1.02	0.34	0.36
AVB-3	70	69	1	1.04	0.34	0.35
LS-1	74	75	/	/	0.34	0.34
LS-2	74	75	/	/	0.34	0.35
LS-3	74	74	/	/	0.34	0.35

Abbreviations: LS: Lattice structure; AVB: Artificial vertebral body.

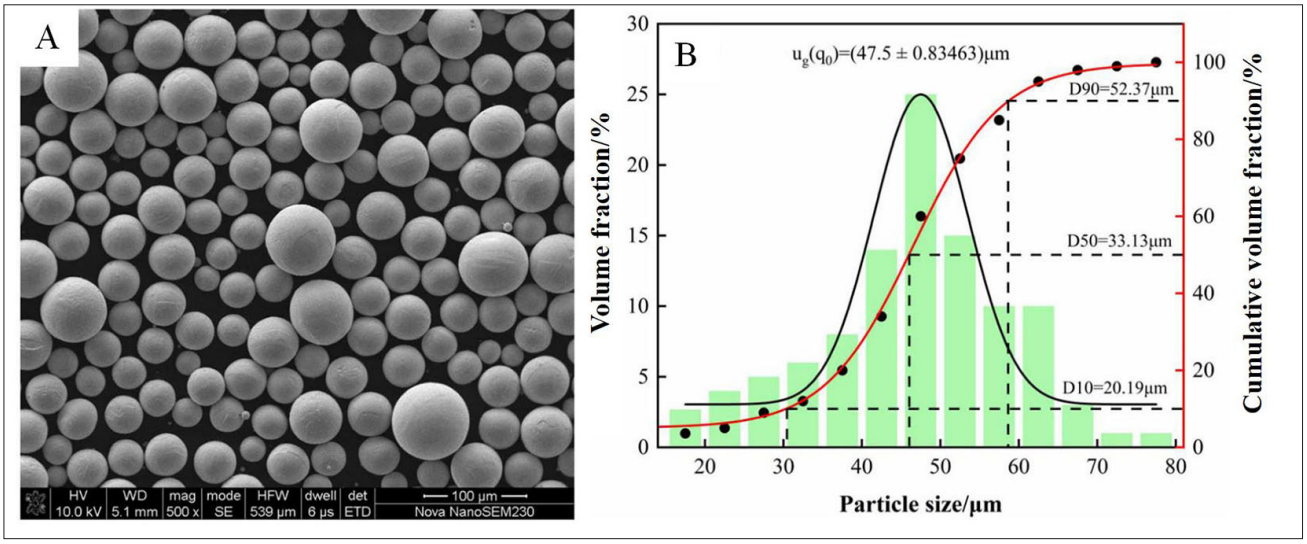

Figure 3. Microstructure (A) and particle size distribution (B) of spherical pure tantalum powder particles used in selective laser melting. Magnification = 500×; scale bar = 100 μm.

Table 2. Chemical composition of the tantalum powder

Elements (wt%)	O	N	C	H	Nb	Mo
	0.021	0.0018	0.0009	0.001	0.001	0.010
	Ti	**Si**	**Fe**	**Ni**	**W**	**Ta**
	0.0013	0.0018	0.0018	0.001	0.009	99.95

Abbreviations: C: Carbon; Fe: Ferrum; H: Hydrogen; Mo: Molybdenum; N: Nitrogen; Nb: Niobium; Ni: Nickel; O: Oxygen; Si: Silicon; Ta: Tantalum; Ti: Titanium; W: Tungsten.

Table 3. Selective laser melting printing parameters

Parameters	Value
Scanning speed	650 mm/s
Laser power	350 W
Layer thickness	0.03 mm
Hatch distance	0.08 mm
Rotation between layers	67°

were within the range of 69%–71%, which was close to the design value of 70%. The porosities of specimens LS-1, LS-2, and LS-3 ranged from 74% to 75%, which was similar to the design value of 74%. The deviations in the actual values of the wall thickness and strut diameter from the design values were less than 10%.

The microscopic morphologies of the AVB specimens are illustrated in Figure 4. The surface and cross-section of the specimens were free of cracks, pores, and unfused defects. A small number of incompletely melted Ta powder particles adhered to the surface of the specimens, which caused a slight deviation in the printing and design dimensions.

2.4. Compression testing

A mechanical universal testing machine (E44 304, MTS, USA) was used to conduct the compressive tests on the specimens. The compression direction was parallel to the specimen building orientation. The loading rate was set to 1 mm/min according to ISO 13314: 2011. A video camera was used to record the deformation of the specimens during compression. The test was terminated when the compression process reached the densification stage. Stress (σ^*) and strain (ε) can be calculated as follows:

$$\begin{cases} \sigma^* = \dfrac{F}{A_0} \\ \varepsilon = \dfrac{\delta}{H} \end{cases} \quad \text{(X)}$$

where F is the loading force, A_0 is the area of the specimen's end face, and H is the height of the specimen. The elastic modulus (E^*) of the specimen was obtained

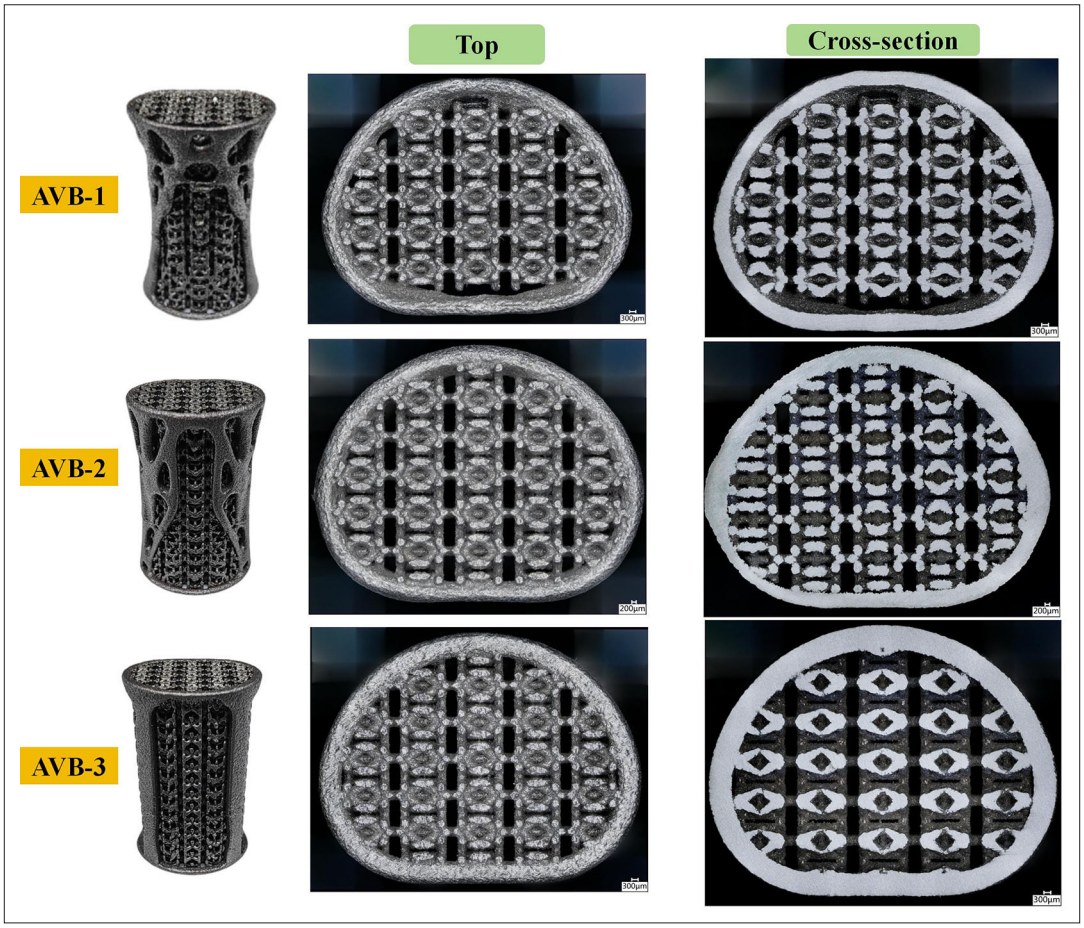

Figure 4. Surface and cross-sectional micromorphologies of tantalum AVBs prepared using selective laser melting. Magnification = 200×; scale bar = 300 μm. Abbreviation: AVB: Artificial vertebral body.

by calculating the slope of the linear elastic phase in the stress–strain curve. The compressive 0.2% offset stress was defined as the yield strength (σ^*_y).

2.5. Finite element analysis

Altair SimSolid (Altair Engineering Inc., USA) was used to simulate the compression of the specimens. SimSolid is a meshless structural analysis software that significantly improves the efficiency of the analysis. The SimSolid computational engine is based on breakthrough extensions of the theory of external approximations, which is an extension of the finite element method. SimSolid can perform the same analyses as other commonly used finite element analysis tools.[55] Previous studies have demonstrated the feasibility and accuracy of SimSolid for analyzing the mechanical properties of bone implants.[56,57]

The finite element model consisted of an upper compression plate, the AVB, and a lower compression plate. The AVB model was placed at the center of the upper and lower plates, as shown in Figure 5. The material properties of Ta were assigned to the AVB model, with an elastic modulus of 186 GPa, Poisson's ratio of 0.35, and a density of 16.6 g/cm^3. The contact conditions between the AVB and plates were set as bonded. The boundary condition specified that the bottom surface of the lower plate was fully constrained, and a displacement along the negative direction of the *z*-axis was applied to the top surface of the upper plate. The sides of the AVB were assigned free boundary conditions. The solution settings and structural analysis were configured to accommodate both stress and material nonlinearity, respectively.

3. Results

3.1. Mechanical properties

The stress–strain curves of typical porous structures, Ta lattice structures, and AVBs under compression are shown in Figure 6. The stress–strain curve can be divided into three phases: linear elastic, plastic deformation, and densification. In the linear elastic phase, stress increases linearly with strain, and the specimen deforms elastically.

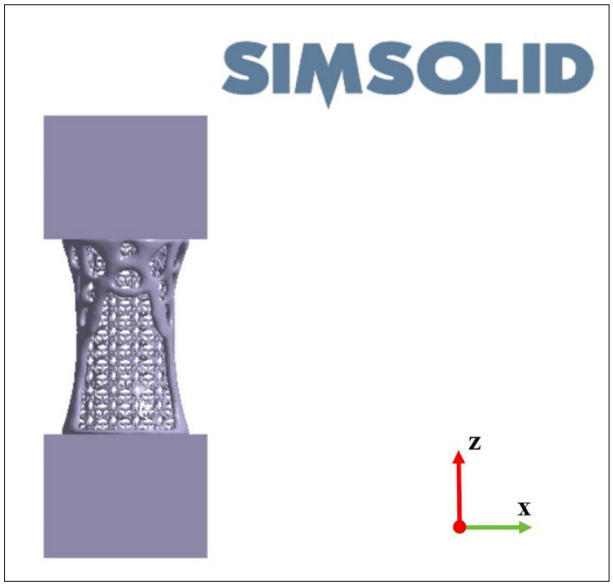

Figure 5. Finite element modeling of the compression process of a tantalum artificial vertebral body.

Upon reaching the yield strength, the specimen enters the plastic deformation phase.

As shown in Figure 6B, during the plastic deformation phase, the stress–strain curves of LS-1, LS-2, and LS-3 are generally smooth, with stress drops observed in regions ①, ②, and ③. In Figure 6C, the stress–strain curve for AVB-1 is smooth, while AVB-2 displays stress oscillations in regions ① and ②. AVB-3 shows a significant decrease in stress after yielding (region ③), but no further stress oscillations occurred during subsequent compression.

The yield strength determines the load-bearing capacity of the AVB, and the elastic modulus dictates its stress-shielding effect from the surrounding bone tissue. Therefore, a higher yield-strength-to-elastic-modulus ratio of the AVB indicates better load-bearing performance while reducing the stress shielding effect. The yield-strength-to-elastic-modulus ratio is calculated as follows:

$$\gamma = \frac{\text{Yield strength}}{\text{Elastic modulus}} = \frac{\sigma_y^* \left(\text{MPa}\right)}{E^* \left(\text{MPa}\right)} \quad \text{(XI)}$$

The elastic modulus, yield strength, and yield-strength-to-elastic-modulus ratio for the Ta lattice structure are shown in Figure 7. The elastic moduli of the LS-1, LS-2, and LS-3 were 1.75, 2.39, and 3.21 GPa, respectively, with yield strengths of 31, 51, and 65 MPa. Despite similar porosities, their elastic moduli and yield strengths varied significantly. This indicates that sidewall curvature has a significant effect on the mechanical properties of the lattice structure. The elastic modulus and yield strength of the lattice structure increased as the sidewall curvature decreased. The yield-strength-to-elastic-modulus ratios for LS-2 and LS-3 (0.021 and 0.02, respectively) were higher than those of LS-1 (0.018).

The elastic modulus, yield strength, and yield-strength-to-elastic-modulus ratios of the Ta AVBs are shown in Figure 8. The elastic moduli of AVB-1, AVB-2, and AVB-3 were 4.38, 5.32, and 12.1 GPa, respectively, with yield strengths of 107, 153, and 235 MPa, respectively. Compared to LS-1, LS-2, and LS-3, AVB-1, AVB-2, and AVB-3 exhibited substantially higher elastic moduli and yield strengths. This indicates that the topological thin-walled structure can significantly improve the load-bearing capacity of the lattice structure. Similar to the lattice structures, reducing the sidewall curvature of AVBs could enhance their load-bearing capacity. AVB-2 had the highest yield-strength-to-elastic-modulus ratio (0.029), which was significantly higher than that of AVB-1 and AVB-3 (0.024 and 0.019, respectively). Zhang et al.[58] successfully fabricated a Ti6Al4V AVB featuring a dual-graded lattice structure using SLM. The dual-grade porous AVB exhibited an elastic modulus of 2631.1 MPa and a yield strength of 53.13 MPa. Notably, the yield-strength-to-elastic-modulus ratio of 0.020 for this artificial vertebra closely resembles that of AVB-3. In contrast, the solid PEEK artificial vertebrae, developed by Wang and colleagues[59] using fused deposition modeling, achieved a yield strength of 94 MPa. Furthermore, the yield strengths of the diamond-lattice PEEK and PEEK/carbon-fiber cages with 48% porosity, as designed by Zhang et al.,[60] were 162 and 118 MPa, respectively, approximating the

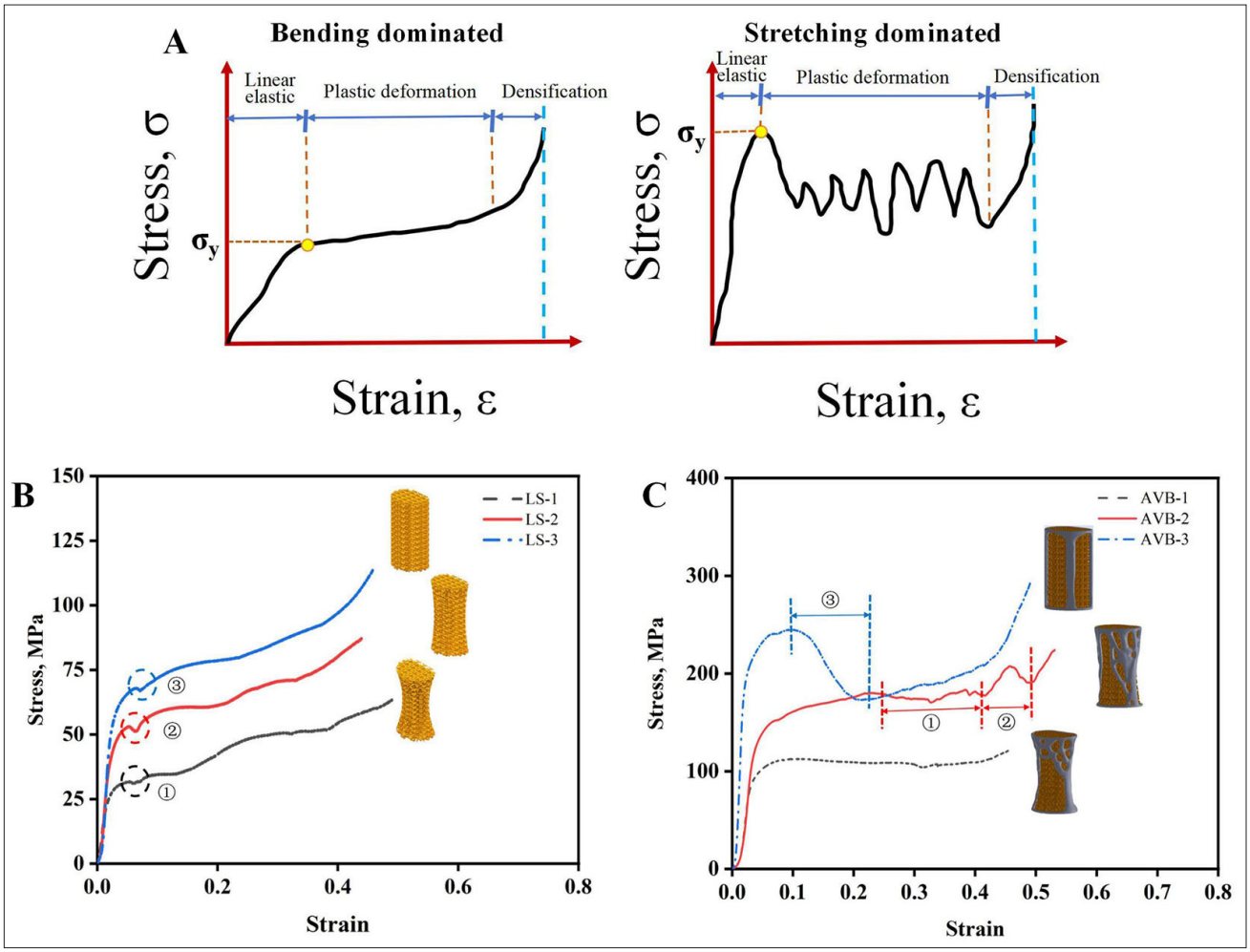

Figure 6. Stress–strain response curves of selective laser melting-printed tantalum lattice structure and artificial vertebral body specimens during compression: (A) elastic–plastic porous structure model, (B) tantalum lattice structures, and (C) tantalum artificial vertebral bodies. Abbreviations: LS: Lattice structure; AVB: Artificial vertebral body.

yield strength of human cortical bone. The Ti6Al4V multi-segment AVB, fabricated by Kang and colleagues,[3] demonstrated a maximum compressive load capacity of 72.72 kN, significantly surpassing that of AVB-1, AVB-2, and AVB-3. This enhanced performance is attributed to its thin-wall thickness of 1.5 mm, which is considerably greater than the 0.5–1.0 mm thickness employed in this study.

3.2. Deformation and failure behavior

The deformation behaviors of LS-1, LS-2, and LS-3 under different strains during the compression tests are shown in Figures 9–11. The Ta lattice structures (LS-1, LS-2, and LS-3) were composed of periodically arranged ISS unit cells. An inclined strut is an essential component of the ISS unit cell. Under external loading, the inclined struts underwent bending deformation caused by bending moments and formed plastic hinges near the nodes, leading the lattice structure to collapse. The unit cells in the middle of the LS-1 and LS-2 specimens deformed first, and their orientations were not inclined. LS-3 maintained a uniform deformation in the XOZ plane, and an X-shaped shear band appeared in the YOZ plane. The unit cells within the shear band deformed first, and the orientations of the peripheral unit cells in the specimen were inclined. Specimens LS-1, LS-2, and LS-3 exhibited varying degrees of expansion during compression, with LS-3 exhibiting the most pronounced expansion.

The deformation behaviors of the AVB-1, AVB-2, and AVB-3 with different strains are shown in Figures 12–14. The deformation behaviors of the Ta AVBs were determined by the deformation of the topological thin-walled and lattice structures, as well as the interaction between them.

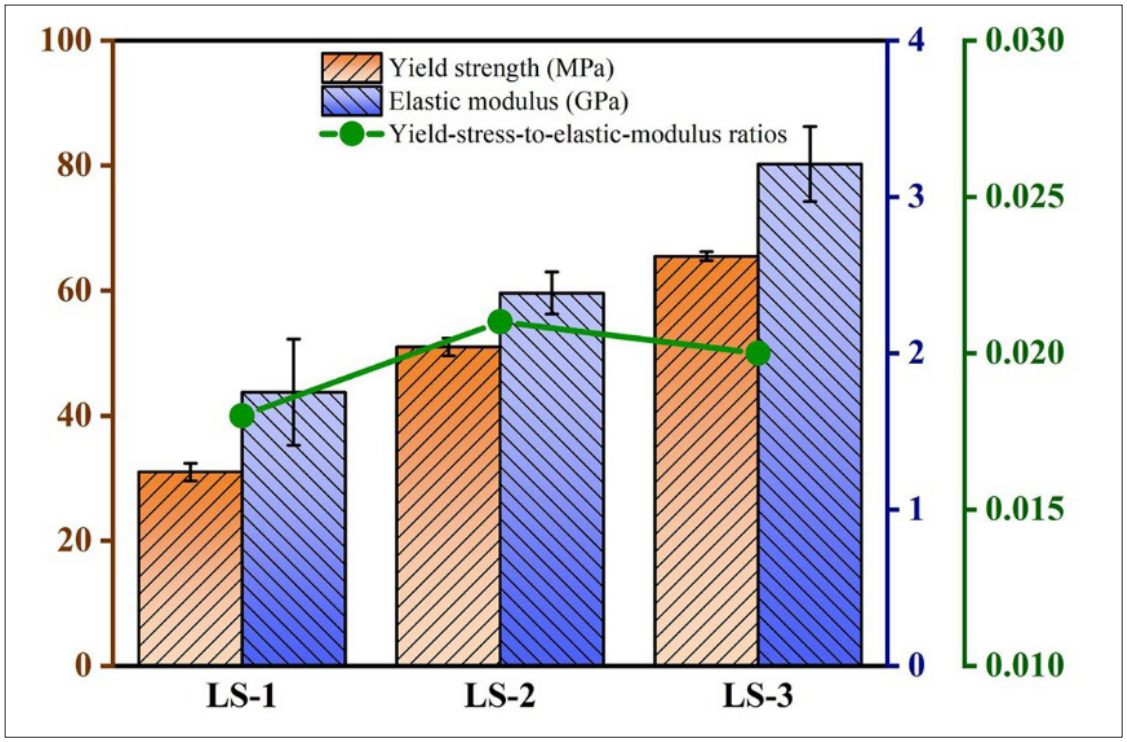

Figure 7. Yield strength, elastic modulus, and yield-stress-to-elastic-modulus ratios of selective laser melting-printed LSs during compression. Abbreviation: LS: Lattice structure.

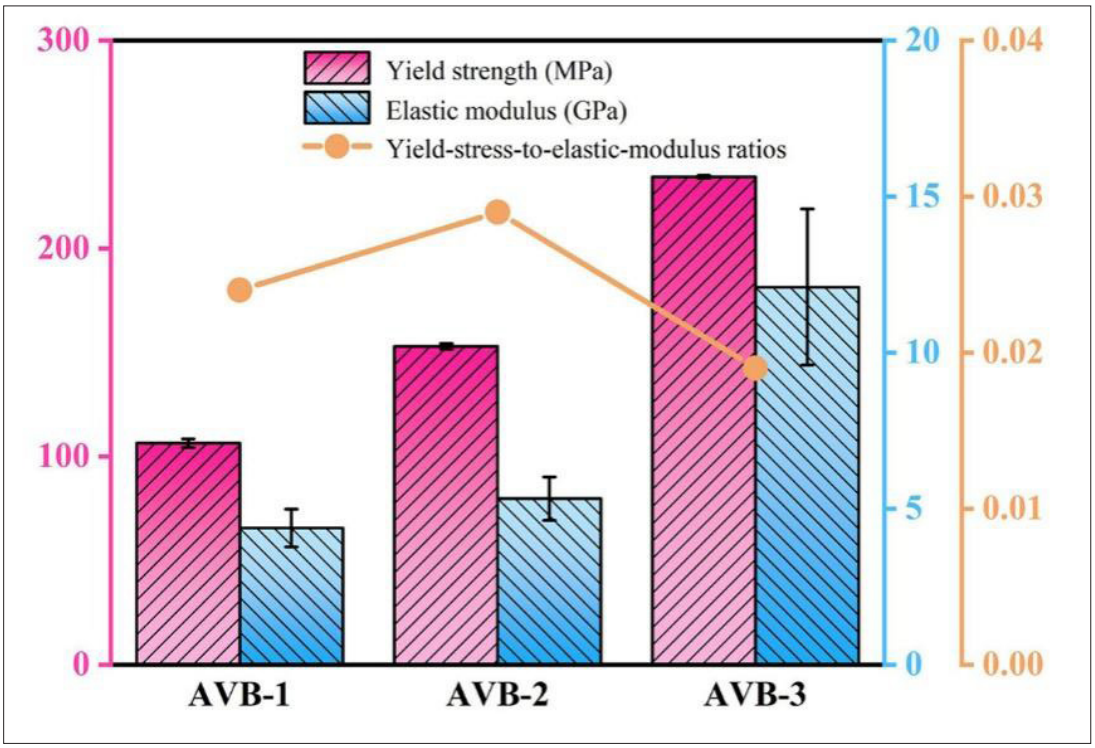

Figure 8. Yield strength, elastic modulus, and yield-stress-to-elastic-modulus ratios of selective laser melting-printed tantalum AVBs during compression. Abbreviation: AVB: Artificial vertebral body.

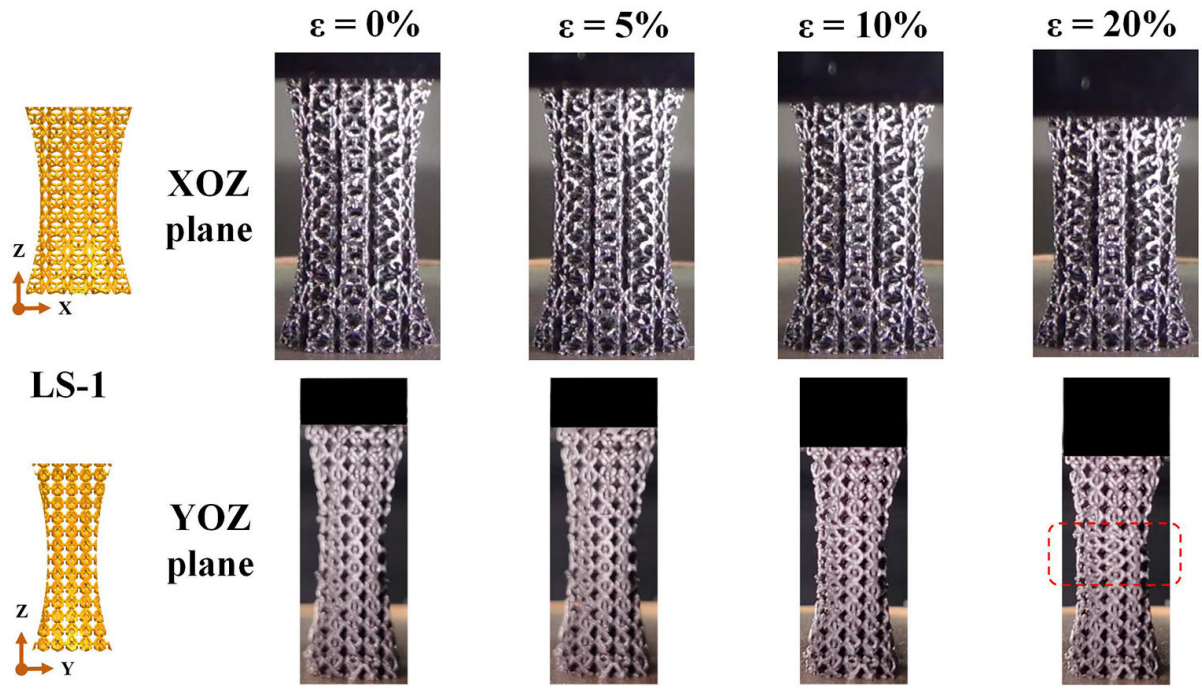

Figure 9. Deformation behavior and failure characteristics of the tantalum LS-1 in the XOZ and YOZ observation planes at 0%, 5%, 10%, and 20% strains. Abbreviation: LS: Lattice structure.

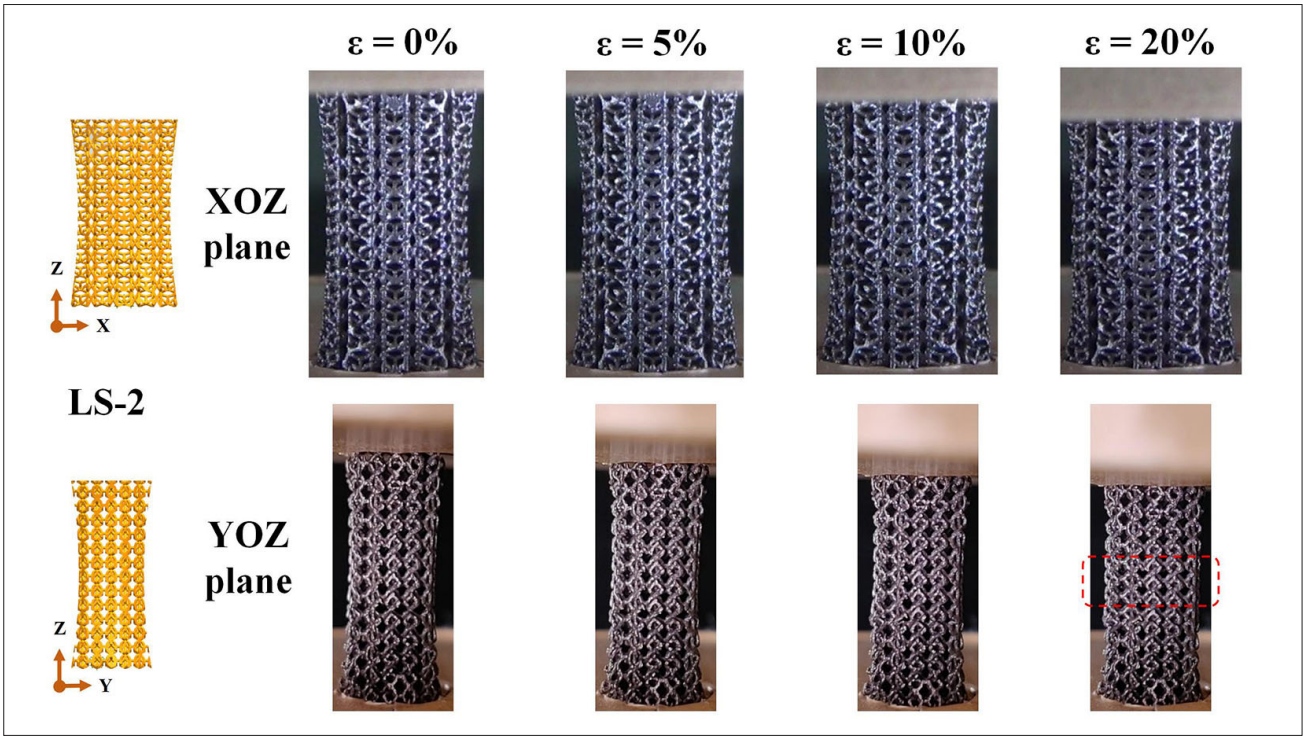

Figure 10. Deformation behavior and failure characteristics of the tantalum LS-2 in the XOZ and YOZ observation planes at 0%, 5%, 10%, and 20% strains. Abbreviation: LS: Lattice structure.

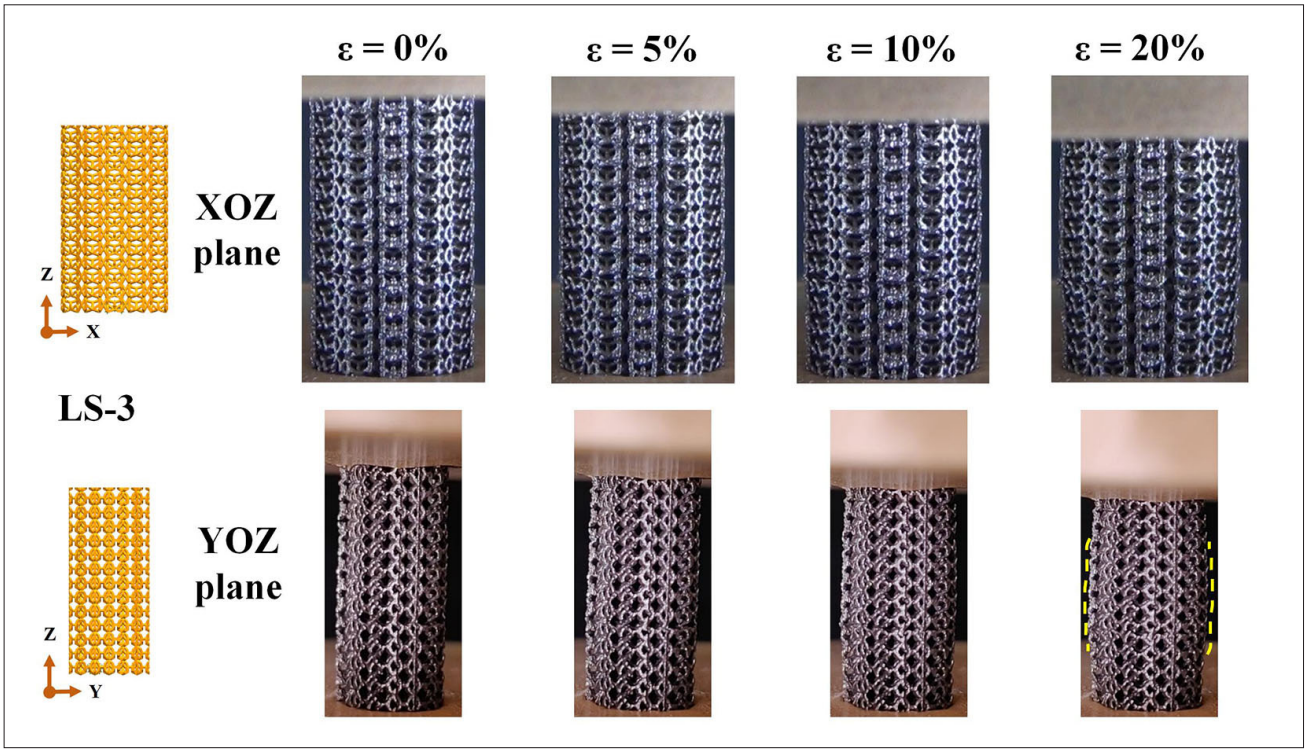

Figure 11. Deformation behavior and failure characteristics of the tantalum LS-3 in the XOZ and YOZ observation planes at 0%, 5%, 10%, and 20% strains. Abbreviation: LS: Lattice structure.

As shown in Figure 12, the topological thin-wall of AVB-1 exhibited "S"- and "C"-shaped bending deformations in the XOZ and YOZ planes, respectively. Similarly, AVB-2 underwent "C"-shaped bending deformation in both the XOZ and YOZ planes (Figure 13). In areas ① and ② of Figure 14, the topological thin wall of AVB-3 buckled in the XOZ and YOZ planes, unlike AVB-1 and AVB-2.

The finite-element simulation results of the compression process for the lattice structures and AVB specimens are shown in Figures 15 and 16, respectively. The deformation modes of the lattice structures and AVBs predicted by finite element simulation were consistent with the experimental outcomes. As shown in Figure 15, LS-1 exhibited instability due to larger sidewall curvature and fewer unit cells in the middle, compared to LS-2 and LS-3. The von Mises stress was concentrated in the middle of LS-1 and LS-2, while no significant stress concentration was observed in LS-3. Figure 16 shows that the main struts of the topologically thin walls in AVB-1 and AVB-2 underwent bending deformation, whereas those in AVB-3 underwent buckling deformation, in agreement with the test results. Significant stress concentrations were revealed in the regions with the most severe deformations of the topologically thin wall and lattice structure. In the YOZ plane, the topologically thin walls and lattice structures of AVB-1, AVB-2, and AVB-3 deformed in the same direction. This indicates that the interaction forces between the topological thin-walled and lattice structures have a significant effect on the mechanical properties and deformation behavior of the AVB.

4. Discussion

The main factors determining the stress–strain response of the Ta lattice structure and AVB are material properties, structure type, and deformation mode. The stress–strain curves of LS-1, LS-2, and LS-3 were smooth in the plastic deformation stage without obvious stress oscillations due to the toughness of Ta and the bending-dominated nature of ISS.[53] During compression of the lattice structures, individual incomplete unit cell positions tended to fill in adjacent voids, resulting in stress reduction in regions ①, ②, and ③ of the stress–strain curves for LS-1, LS-2, and LS-3 (Figure 6B).

TTS-1 and TTS-2 had sidewall curvatures of 0.027 and 0.014 mm^{-1}, respectively, and underwent bending deformation during compression. Meanwhile, LS-1 and LS-2 were bending-dominant lattice structures. Therefore, AVB-1 and AVB-2 belong to the bending-dominated type of porous structure, and their stress–strain curves were

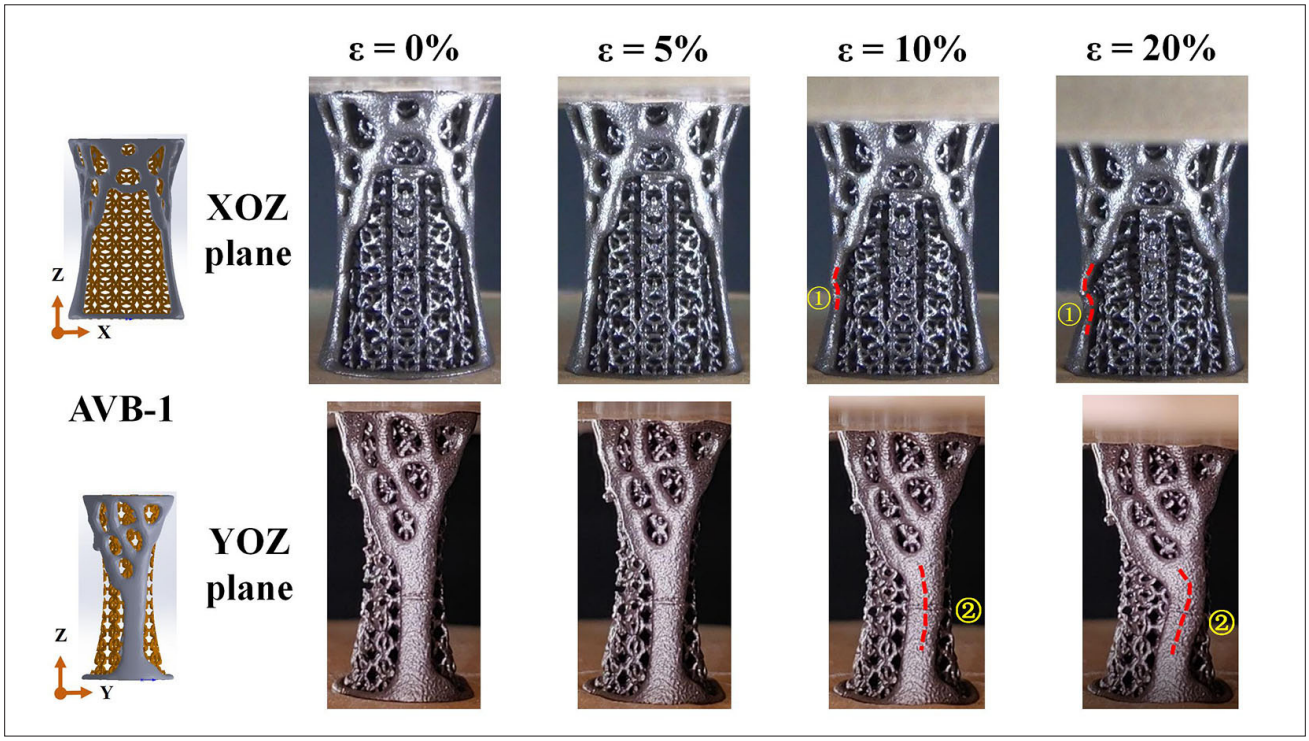

Figure 12. Deformation behavior and failure characteristics of the tantalum AVB-1 in the XOZ and YOZ observation planes at 0%, 5%, 10%, and 20% strains. Abbreviation: AVB: Artificial vertebral body.

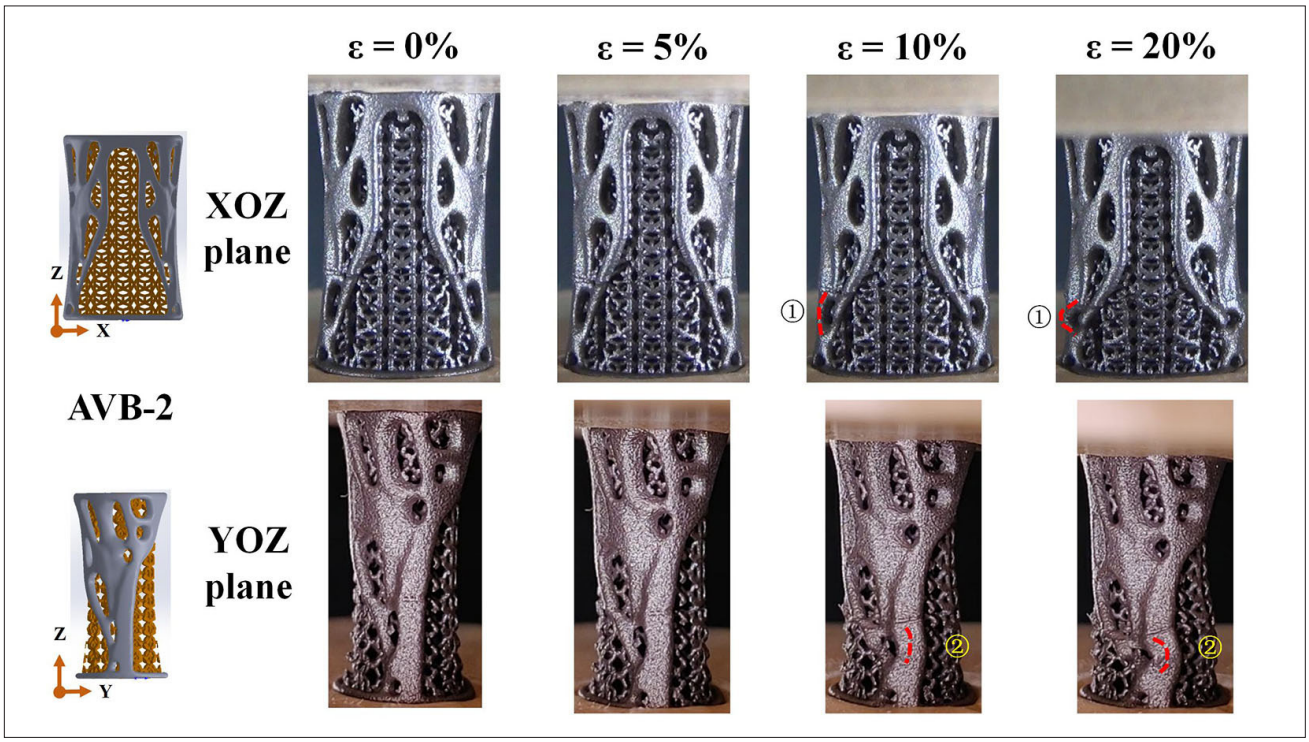

Figure 13. Deformation behavior and failure characteristics of the tantalum AVB-2 in the XOZ and YOZ observation planes at 0%, 5%, 10%, and 20% strains. Abbreviation: AVB: Artificial vertebral body.

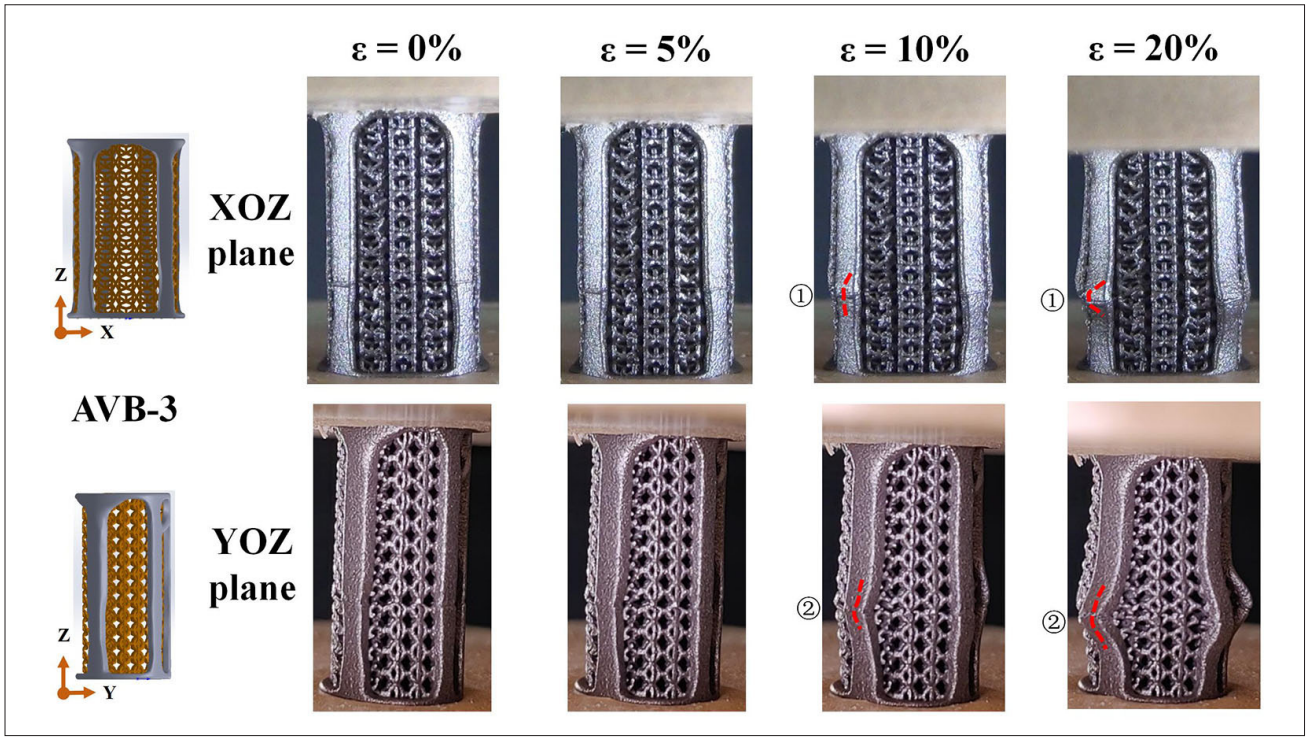

Figure 14. Deformation behavior and failure characteristics of the tantalum AVB-3 in the XOZ and YOZ observation planes at 0%, 5%, 10%, and 20% strains. Abbreviation: AVB: Artificial vertebral body.

smooth overall in the plastic deformation stage without stress oscillation, as shown in Figure 6C. Regions ① and ② in the stress–strain curve of AVB-2 correspond to the plastic deformation of the topologically thin wall. The stress reduction in region ① was attributed to the topological thin wall peeling off from the internal lattice structure. As the strain increased, the topologically thin wall fractured at the location with the greatest degree of bending, causing a stress reduction in region ②.

The topological thin-walled structure of AVB-3 consisted of vertical struts, which were stretching-dominated. The lattice structure consisted of ISS unit cells, which were bending-dominated. Therefore, the stress–strain curve of AVB-3 combines the characteristics of stretching-dominated and bending-dominated porous structures. The buckling deformation of the topologically thin wall, its separation from the lattice structure, and subsequent fracture significantly reduced the stress during the plastic deformation phase (region ③). After the fracture of the topologically thin wall of AVB-3, the bending-dominated lattice structures became the main load-bearing components. As a result, the subsequent compression process yielded smooth curves without stress oscillations until the sample was densified, as exhibited in Figure 6C.

When the unit cells fill the limited space and form lattice structures with varying sidewall curvatures, maintaining the same porosity for LS-1, LS-2, and LS-3 requires sacrificing the integrity of some unit cells. Consequently, these compromised unit cells cannot fully exhibit their load-bearing capabilities. Reducing the sidewall curvatures of the solid model results in an increase in the filling space, thereby enhancing the number of unit cells within the lattice structure. The number of intact unit cells in LS-1, LS-2, and LS-3 was 117, 195, and 247, respectively. Therefore, as depicted in Figure 7, LS-3 exhibited the highest yield strength and elastic modulus.

The sidewall struts of TTS-1 and TTS-2 were bending-dominant. As the sidewall curvature increased, the angle between the struts and the horizontal decreased, leading to a reduction in both strength and elastic modulus. When the sidewall curvature was zero, the thin wall of TTS-3 consisted of vertical struts with stretching-dominated mechanical properties, which significantly enhanced the load-bearing capacity of the AVB. However, the sidewall curvature had a different effect on the forces between the lattice and topological thin-walled structures.

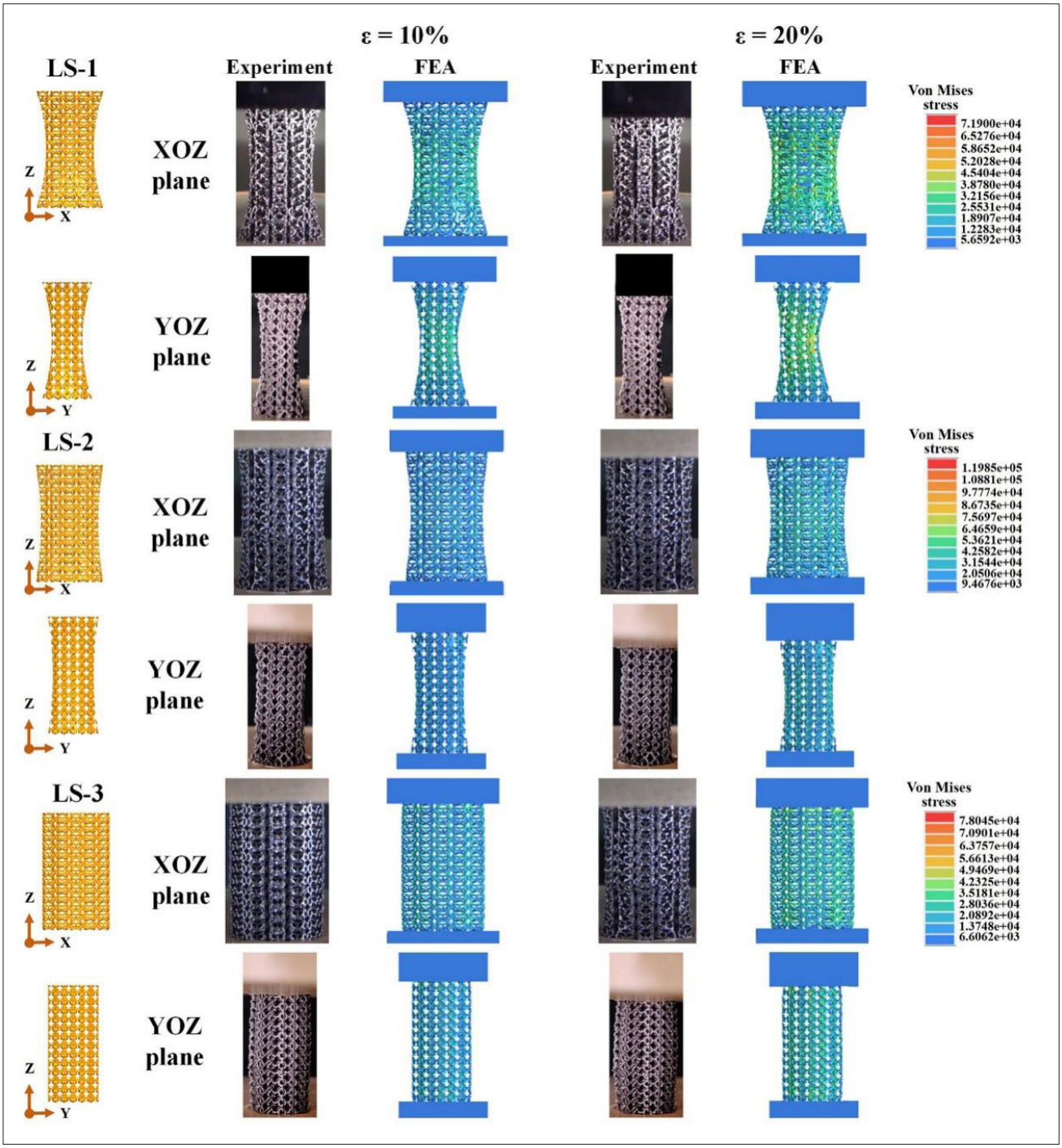

Figure 15. Comparison of experimental and FEA results for tantalum LSs at 10% and 20% strain in the XOZ and YOZ observation planes. Abbreviations: LS: Lattice structure; FEA: Finite element analysis.

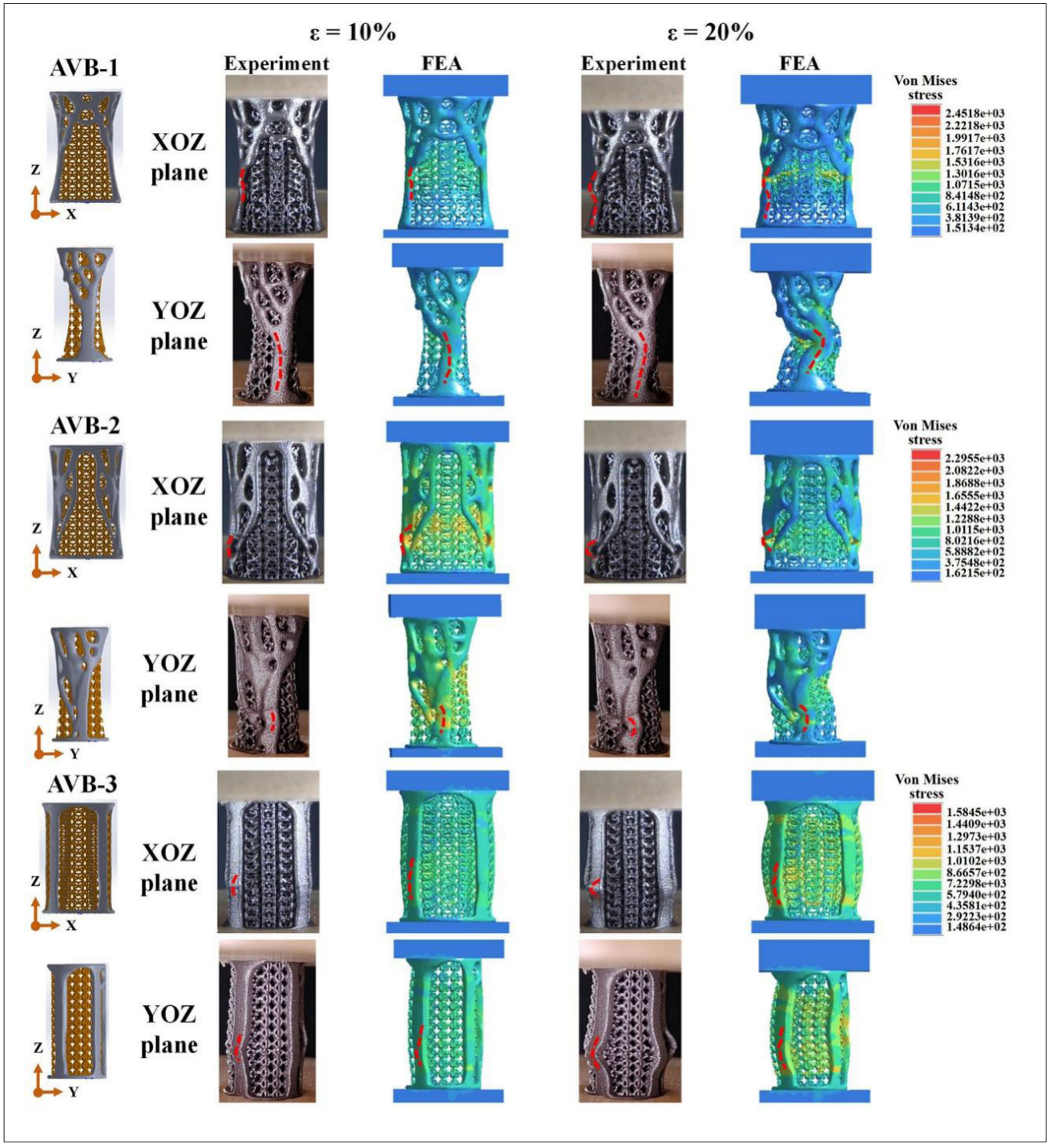

Figure 16. Comparison of experimental and FEA results for tantalum AVBs at 10% and 20% strain in the XOZ and YOZ observation planes. Abbreviations: AVB: Artificial vertebral body; FEA: Finite element analysis.

The absence of horizontal orientation constraints caused the lattice structure to expand outward during compression. The force and deformation characteristics of topological thin-walled and artificial vertebral samples during compression are displayed in Figure 17. The topological thin-walled structures of AVB-1 and AVB-2 featured specific sidewall curvatures, which led to the formation of plastic hinges at the center of the sidewall under compression. The inward bending of the topological thin-walled structure created an interaction force with the outwardly expanding lattice structure, as shown in Figure 17. In other words, the topological thin-walled structure restricted the inclination of the peripheral unit cells of the lattice structure, imposing horizontal constraints on the internal lattice and inhibiting its outward expansion. The interaction force between the topological thin-walled and lattice structures in AVB-1 and AVB-2 enhanced both the elastic modulus and the yield strength of the AVB. An increase in sidewall curvature led to a higher interaction force, thereby enhancing the load-bearing capacity of the AVB.

The topologically thin wall of AVB-3 consisted of vertical struts with zero sidewall curvature. As depicted in Figure 17, the outward expansion of the lattice structures provided a source of perturbation for vertical strut buckling during compression. This accelerated the buckling deformation of the vertical struts, thereby reducing the load-bearing capacity of the AVB. Therefore, sidewall curvature had different effects on the elastic modulus and yield strength of the AVB. The focus of this study was to regulate sidewall curvature to develop an AVB exhibiting optimal mechanical properties.

After implantation, the AVB was osseointegrated with the upper and lower cervical vertebral segments, thereby performing a load-bearing function and restoring intervertebral height. An AVB requires adequate yield strength, and its elastic modulus should closely match that of human bone. This reduces the risk of stress shielding and promotes osseointegration. The elastic modulus and yield strength of human cortical bone range from 7.7 to 21.8 GPa and 103 to 222 MPa, respectively.[27] The yield strengths of AVB-1, AVB-2, and AVB-3 were within the range of human cortical bone yield strength. This demonstrated that the load-bearing capacities of AVB-1, AVB-2, and AVB-3 met the requirements for the replacement of diseased vertebrae. As exhibited in Figure 8, compared to AVB-1 and AVB-3, AVB-2 exhibited the highest yield-strength-to-elastic-modulus ratio. This design effectively reduced the stress shielding effect while maximizing the load-bearing function.

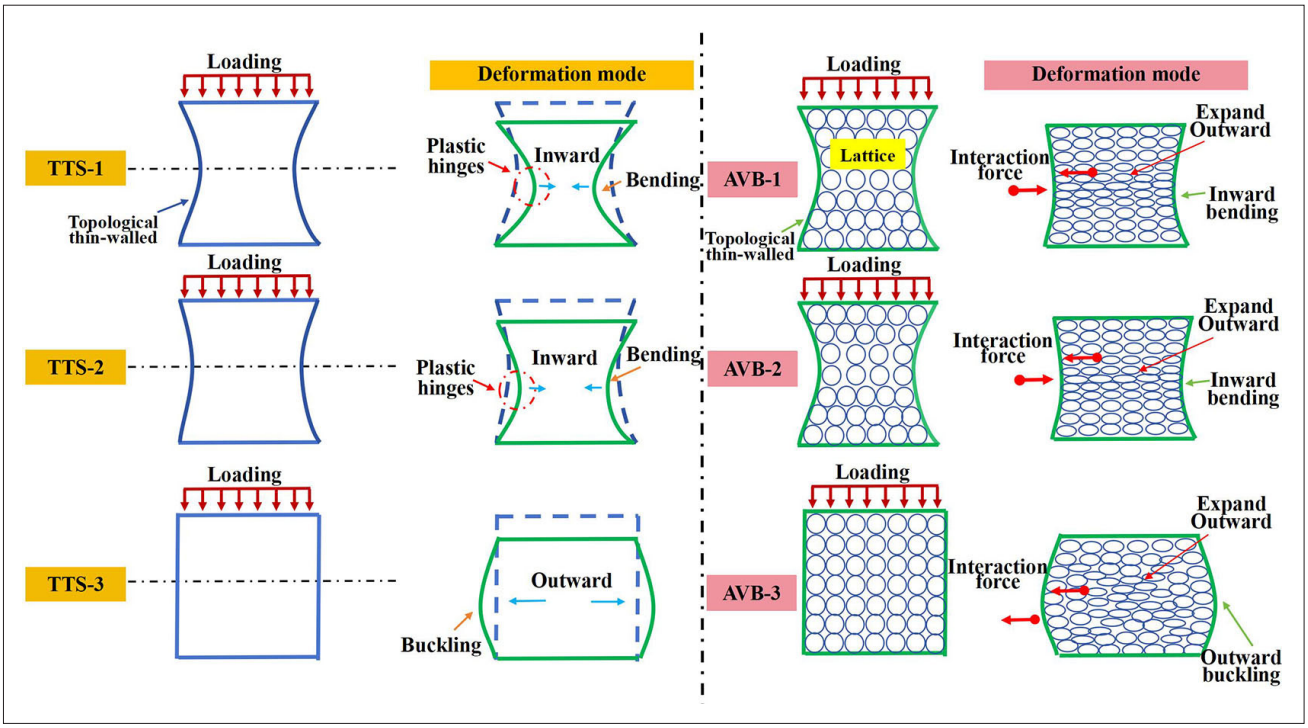

Figure 17. Schematic representation of the force and deformation characteristics of TTSs and AVBs. Abbreviations: AVB: Artificial vertebral body; TTS: Topologically thin-walled structure.

The topological thin-walled TTS-3 consisted of vertical struts that significantly enhanced the elastic modulus and yield strength of AVB-3. However, owing to TTS-3's insufficient constraint on the expansion deformation of the lattice structure during compression, the vertical struts buckled, and the thin-walled structure exhibited premature yielding (Figure 17). This resulted in the lowest yield-strength-to-elastic-modulus ratio of AVB-3. Because the sidewall curvature of the topologically thin wall in AVB-1 was larger than that in AVB-2, the interaction force between the topologically thin wall and the lattice structure in AVB-1 was greater than that in AVB-2. This interaction force exerted a more pronounced enhancement on the elastic modulus than on the yield strength. Therefore, as shown in Figure 8, the yield-strength-to-elastic-modulus ratios of AVB-2 were higher than those of AVB-1. AVB-2, with a sidewall curvature of 0.014 mm^{-1}, has potential for clinical application because it can meet the daily load-bearing requirements of the human cervical spine while reducing the risk of stress shielding.

Ti mesh is widely used in the clinical treatment of spinal tumors owing to its simple structure. Although Ti mesh is effective for spinal reconstruction, it is poorly adapted to vertebral bone in terms of size, shape, and mechanical properties, which seriously affects the therapeutic effect. Surgeons need to cut the Ti mesh size on-site according to the patient's intervertebral height during the surgery, resulting in an increase in surgical time and difficulty. The shape of the end face of the Ti mesh cannot match the curvature of the end plate, leading to stress concentration at the contact surface between the Ti mesh and the end plate, thereby increasing the risk of subsidence. Moreover, the Ti mesh has an insufficient load-bearing capacity, and most of the load is carried by the fixation system, which produces stress shielding of the contacted vertebrae, resulting in bone resorption and stress collapse. According to clinical reports, there are still a large number of cases of poor osseointegration, inadequate immediate and long-term stability, and short *in vivo* survival cycles after Ti mesh implantation.[21,61,62]

In this study, the Ta artificial vertebra was custom-designed based on the shape and anatomical dimensions of the vertebrae of a specific patient. The height of the AVB remained the same as the intervertebral height, avoiding on-site adjustment and reducing the difficulty of surgery. The upper and lower end faces of the customized artificial vertebrae can be accurately fitted to the endplate, thereby reducing stress concentration at the contact interface and lowering the risk of subsidence. Meanwhile, AVB-2 exhibited the highest yield-strength-to-elastic-modulus ratio, which could prevent excessive load transfer along the fixation system and reduce the stress shielding effect. Therefore, AVB-2 has a lower risk of subsidence than conventional Ti mesh in clinical applications.

The deformation behavior of AVBs was closely related to their mechanical properties. The sidewall curvatures of the LS-1 and LS-2 specimens were 0.027 and 0.014 mm^{-1}, respectively, resulting in a reduced number of intact unit cells in the central region compared with the upper and lower sections of the specimens. This explains why the unit cells in the middle of specimens LS-1 and LS-2 deformed first during compression, as depicted in Figures 9 and 10. The reason for the appearance of the shear band in the YOZ plane of the LS-3 specimen (Figure 11) was that the maximum shear stress formed at an angle of 45° to the axial compression direction. The unit cells in this shear band deformed first. The asymmetry of the ISS unit cell prevented the formation of a shear band in the XOZ plane of the LS-3 specimen.

In the Ta AVB specimen, the material density distribution of the topologically thin wall significantly influenced its deformation behavior. During the load transfer process, the area with the highest material density in the topological thin wall exhibited the highest load-carrying capacity and lowest deformation tendency. In contrast, areas with lower material density showed diminished load-carrying capacity and a tendency to yield prematurely. As shown in Figures 12 and 13, along the *z*-axis direction of the specimens, the material densities in regions ① and ② of the topologically thin walls in AVB-1 and AVB-2 varied. The material density in the upper part of these regions was greater than that in the lower part. Consequently, plastic hinges formed first in these regions, resulting in bending deformation.

The topologically thin walls of the AVB-3 specimen experienced failure as a result of plastic deformation in regions ① and ②, as displayed in Figure 14. The topologically thin wall of AVB-3 comprised vertical struts and exhibited no variation in material density in regions ① and ②. Under compressive loading, the internal lattice expanded outward, acting as a perturbation source for vertical strut buckling and accelerating the instability of the topologically thin wall (Figure 17).

As exhibited in Figure 16, the finite element results indicated that the stress concentrations were localized in areas with alternating material densities within the topologically thin walls of AVB-1 and AVB-2 (regions ① and ②). AVB-3 displayed pronounced stress concentrations at locations where the vertical struts buckled. This stress accumulation initially caused the structure in these areas to deform.

5. Conclusion

Novel AVB models were designed through topology optimization, and Ta AVBs were successfully manufactured using the SLM process. The effects of sidewall curvature on the mechanical properties and deformation mechanisms of the Ta AVB were investigated using compression tests and finite element analysis. The conclusions are as follows.

The elastic modulus and yield strength of the Ta lattice structures ranged from 1.75 to 3.21 GPa and 31 to 65 MPa, respectively. With the addition of topologically thin walls, the elastic modulus and yield strength were enhanced by factors of 2.26–3.77 and 3–3.62, respectively. Topological thin-walled structures can significantly increase the load-bearing capacity of the lattice structures.

As the sidewall curvature decreased, the elastic modulus and yield strength of the AVB increased. When the sidewall curvature decreased from 0.027 to 0 mm^{-1}, the elastic modulus and yield strength of the Ta AVB increased by factors of 2.76 and 2.19, respectively.

The yield strengths of the Ta AVBs (ranging from 107 to 235 MPa) were similar to those of the human cortical bone (103–222 MPa). AVB-2 exhibited the highest yield-strength-to-elastic-modulus ratio (0.029) compared to that of AVB-1 and AVB-3 (0.024 and 0.019, respectively). This indicated that the optimal sidewall curvature of the topological thin wall is 0.014 mm^{-1}. At this sidewall curvature, the Ta AVB effectively reduced the stress shielding effect while maximizing the load-bearing function. Therefore, AVB-2 not only fully exerted its load-bearing function but also has the potential to promote osseointegration and reduce the risk of bone absorption in cervical fusion segments and degenerative diseases in adjacent segments.

The deformation modes of the Ta AVB during compression determined its stress–strain response. The deformation modes of AVB-1 and AVB-2 involved the bending deformation of the topologically thin walls and lattice structures. In AVB-3, the compressive expansion effect of the lattice acted as a perturbation source for topological thin-wall buckling, accelerating its collapse.

Finite element analysis is an effective method for predicting and evaluating the biomechanical properties of bone implants in clinical applications. Previous studies have demonstrated the feasibility and accuracy of using the finite element method to evaluate the biomechanical properties of bone implants in human load-bearing sites, such as the hip joints,[63] pelvis,[64] intervertebral discs,[65] knee joints,[66] and lumbar vertebrae.[67] The strain and stress distribution on the AVB significantly affect the contacted vertebrae and adjacent intervertebral discs, articular cartilage, and vertebral bodies. Therefore, finite element analysis of the biomechanics of the Ta AVB in the human spine will be the focus of future research. Furthermore, research on the fatigue performance of Ta AVBs under long-term dynamic loading in the human spine is an important future investigation. The biological properties of Ta artificial vertebra will be verified by *in vivo* and *in vitro* tests in future studies.

Acknowledgments

None.

Funding

This work was supported by the Natural Science Foundation of Xinjiang Uygur Autonomous Region, China under grant number 2023D01A86, the Scientific and Technological Research Projects in Key Areas of Xinjiang Production and Construction Corps, China under grant number 2024ABO49, and the Key Research and Development Program of Xinjiang Uygur Autonomous Region, China under grant number 2023B01016.

Conflict of interest

The authors declare that they have no competing interests.

Author contributions

Conceptualization: Yutao Zhang
Data curation: Jintao Li
Investigation: Yutao Zhang, Jintao Li, Yong Huang, Xiaohong Dong
Methodology: Wurikaixi Aiyiti
Supervision: Wurikaixi Aiyiti
Validation: Yutao Zhang
Writing–original draft: Yutao Zhang, Wurikaixi Aiyiti
Writing–review & editing: Wurikaixi Aiyiti

Ethics approval and consent to participate

Not applicable.

Consent for publication

Not applicable.

Availability of data

The data supporting the findings of this study are available from the corresponding author upon reasonable request.

References

1. Shimizu T, Kato S, Yokogawa N, et al. Total en bloc spondylectomy for primary tumors of the thoracic

and lumbar spine: a review article. *Semin Spine Surg.* 2024;36(4):101137.
doi: 10.1016/j.semss.2024.101137

2. Kandziora F, Schnake KJ, Klostermann CK, Haas NP. Vertebral body replacement in spine surgery. *Unfallchirurg.* 2004;107(5):354-371.
doi: 10.1007/s00113-004-0777-z

3. Kang J, Dong E, Li X, et al. Topological design and biomechanical evaluation for 3D printed multi-segment artificial vertebral implants. *Mater. Sci. Eng. C-Mater. Biol. Appl.* 2021;127:112250.
doi: 10.1016/j.msec.2021.112250

4. Zhang YW, Deng L, Zhang XX, et al. Three-dimensional printing-assisted cervical anterior bilateral pedicle screw fixation of artificial vertebral body for cervical tuberculosis. *World Neurosurg.* 2019;127:25-30.
doi: 10.1016/j.wneu.2019.03.238

5. Perez Roman RJ, Boddu JV, Bashti M, et al. The use of carbon fiber-reinforced instrumentation in patients with spinal oncologic tumors: a systematic review of literature and future directions. *World Neurosurg.* 2023;173:13-22.
doi: 10.1016/j.wneu.2023.01.090

6. Chen G, Yin M, Liu W, et al. A novel height-adjustable nano-hydroxyapatite/polyamide-66 vertebral body for reconstruction of thoracolumbar structural stability after spinal tumor resection. *World Neurosurg.* 2019;122:e206-e214.
doi: 10.1016/j.wneu.2018.09.213

7. Kong F, Nie Z, Liu Z, Hou S, Ji J. Developments of nano-TiO_2 incorporated hydroxyapatite/PEEK composite strut for cervical reconstruction and interbody fusion after corpectomy with anterior plate fixation. *J Photochem Photobiol B-Biol.* 2018;187:120-125.
doi: 10.1016/j.jphotobiol.2018.07.016

8. Abd-Elaziem W, Darwish MA, Hamada A, Daoush WM. Titanium-based alloys and composites for orthopedic implants applications: a comprehensive review. *Mater. Des.* 2024;241:112850.
doi: 10.1016/j.matdes.2024.112850

9. Kurtz SM, Devine JN. PEEK biomaterials in trauma, orthopedic, and spinal implants. *Biomaterials.* 2007;28(32):4845-4869.
doi: 10.1016/j.biomaterials.2007.07.013

10. Ma H, Suonan A, Zhou J, et al. PEEK (Polyether-ether-ketone) and its composite materials in orthopedic implantation. *Arab J Chem.* 2021;14(3):102977.
doi: 10.1016/j.arabjc.2020.102977

11. Liu C, Xu M, Wang Y, et al. Exploring the potential of hydroxyapatite-based materials in biomedicine: a comprehensive review. *Mater Sci Eng R-Rep.* 2024;161:100870.
doi: 10.1016/j.mser.2024.100870

12. Minagar S, Berndt CC, Wang J, Ivanova E, Wen C. A review of the application of anodization for the fabrication of nanotubes on metal implant surfaces. *Acta Biomater.* 2012;8(8):2875-2888.
doi: 10.1016/j.actbio.2012.04.005

13. Jiang H. F, Aihemaiti P, Aiyiti W, Kasimu A. Study of the compression behaviours of 3D-printed PEEK/CFR-PEEK sandwich composite structures. *Virtual Phys Prototyp.* 2022;17(2):138-155.
doi: 10.1080/17452759.2021.2014636

14. Zheng J, Zhao H, Ouyang Z, et al. Additively-manufactured PEEK/HA porous scaffolds with excellent osteogenesis for bone tissue repairing. *Compos Pt B-Eng.* 2022;232:109508.
doi: 10.1016/j.compositesb.2021.109508

15. Li S, Li G, Hu J, et al. Porous polyetheretherketone-hydroxyapatite composite: a candidate material for orthopedic implant. *Compos Commun.* 2021;28:100908.
doi: 10.1016/j.coco.2021.100908

16. Aufa AN, Hassan MZ, Ismail Z. Recent advances in Ti-6Al-4V additively manufactured by selective laser melting for biomedical implants: prospect development. *J Alloy Compd.* 2022;896:163072.
doi: 10.1016/j.jallcom.2021.163072

17. Depboylu FN, Yasa E, Poyraz O, Minguella-Canela J, Korkusuz F, Lopez MAD. Titanium based bone implants production using laser powder bed fusion technology. *J Mater Res Technol.* 2022;17:1408-1426.
doi: 10.1016/j.jmrt.2022.01.087

18. Mirkhalaf M, Men Y, Wang R, No Y, Zreiqat H. Personalized 3D printed bone scaffolds: a review. *Acta Biomater.* 2023;156:110-124
doi: 10.1016/j.actbio.2022.04.014

19. Wu Y, Feng P, Kong Q, et al. Treatment of lumbosacral tuberculosis with significant vertebral body loss using single-stage posterior surgical management with a structural autograft combined with a titanium mesh cage. *World Neurosurg.* 2021;148:e10-e16.
doi: 10.1016/j.wneu.2020.11.104

20. Zhang HQ, Li M, Wang YX, et al. Minimum 5-year follow-up outcomes for comparison between titanium mesh cage and allogeneic bone graft to reconstruct anterior column through posterior approach for the surgical treatment of thoracolumbar spinal tuberculosis with kyphosis. *World Neurosurg.* 2019;127:e407-e415.
doi: 10.1016/j.wneu.2019.03.139

21. Jang J. W, Lee J. K, Lee J. H, Hur H, Kim T. W, Kim S. H. Effect of posterior subsidence on cervical alignment after anterior cervical corpectomy and reconstruction using titanium mesh cages in degenerative cervical disease. *J Clin Neurosci.* 2014;21(10):1779-1785.
doi: 10.1016/j.jocn.2014.02.016

22. Bencharit S, Byrd WC, Altarawneh S, et al. Development and applications of porous tantalum trabecular metal-

enhanced titanium dental implants. *Clin Implant Dent Relat Res.* 2014;16(6):817-826.
doi: 10.1111/cid.12059

23. Piglionico S, Bousquet J, Fatima N, Renaud M, Collart-Dutilleul PY, Bousquet P. Porous tantalum vs. titanium implants: enhanced mineralized matrix formation after stem cells proliferation and differentiation. *J Clin Med.* 2020;9(11):3657.
doi: 10.3390/jcm9113657

24. Li X, Wang L, Yu XM, et al. Tantalum coating on porous Ti6Al4V scaffold using chemical vapor deposition and preliminary biological evaluation. *Mater Sci Eng C-Mater Biol Appl.* 2013;33(5):2987-2994.
doi: 10.1016/j.msec.2013.03.027

25. Wang X, Ning B, Pei X. Tantalum and its derivatives in orthopedic and dental implants: osteogenesis and antibacterial properties. *Colloid Surf B-Biointerfaces.* 2021;208:112055.
doi: 10.1016/j.colsurfb.2021.112055

26. Wang X, Liu W, Jiang C, et al. Research progress on the osteogenic properties of tantalum in the field of medical implant materials. *J Mater Res Technol*. 2024;30:1706-1715.
doi: 10.1016/j.jmrt.2024.03.200

27. Ataee A, Li Y, Brandt M, Wen C. Ultrahigh-strength titanium gyroid scaffolds manufactured by selective laser melting (SLM) for bone implant applications. *Acta Mater.* 2018;158:354-368.
doi: 10.1016/j.actamat.2018.08.005

28. Zhang Y, Yang J, Wan W, et al. Evaluation of biological performance of 3D printed trabecular porous tantalum spine fusion cage in large animal models. *J Orthop Transl.* 2025;50:185-195.
doi: 10.1016/j.jot.2024.10.010

29. Wang X, Xu S, Zhou S, et al. Topological design and additive manufacturing of porous metals for bone scaffolds and orthopaedic implants: a review. *Biomaterials*. 2016;83:127-141.
doi: 10.1016/j.biomaterials.2016.01.012

30. Chen LY, Liang SX, Liu YJ, Zhang LC. Additive manufacturing of metallic lattice structures: unconstrained design, accurate fabrication, fascinated performances, and challenges. *Mater Sci Eng R-Rep.* 2021;146:100648.
doi: 10.1016/j.mser.2021.100648

31. Benedetti M, du Plessis A, Ritchie RO, Dallago M, Razavi SMJ, Berto F. Architected cellular materials: a review on their mechanical properties towards fatigue-tolerant design and fabrication. *Mater Sci Eng R-Rep*. 2021;144:100606.
doi: 10.1016/j.mser.2021.100606

32. Wang Z, Zhang M, Liu Z, et al. Biomimetic design strategy of complex porous structure based on 3D printing Ti-6Al-4V scaffolds for enhanced osseointegration. *Mater Des.* 2022;218:110721.
doi: 10.1016/j.matdes.2022.110721

33. Zhang BQ, Pei X, Zhou CC, et al. The biomimetic design and 3D printing of customized mechanical properties porous Ti6Al4V scaffold for load-bearing bone reconstruction. *Mater Des.* 2018;152:30-39.
doi: 10.1016/j.matdes.2018.04.065

34. Lu HZ, Ma HW, Luo X, et al. Microstructure, shape memory properties, and invitro biocompatibility of porous NiTi scaffolds fabricated via selective laser melting. *J Mater Res Technol.* 2021;15:6797-6812.
doi: 10.1016/j.jmrt.2021.11.112

35. Deng FY, Liu LL, Li Z, Liu JC. 3D printed Ti6Al4V bone scaffolds with different pore structure effects on bone ingrowth. *J Biol Eng.* 2021;15(1):4.
doi: 10.1186/s13036-021-00255-8

36. Guo Z, Wang C, Du C, Sui J, Liu J. Effects of topological structure on antibacterial behavior and biocompatibility of implant. *Procedia CIRP*. 2020;89:126-131.
doi: 10.1016/j.procir.2019.12.003

37. Chen J, Song C, Deng Z, et al. Functional gradient design of additive manufactured gyroid tantalum porous structures: manufacturing, mechanical behaviors and permeability. *J Manuf Process.* 2024;125:202-216.
doi: 10.1016/j.jmapro.2024.07.054

38. Song C, Chen J, Lei H, et al. Radial gradient design enabling additively manufactured low-modulus gyroid tantalum structures. *Int J Mech Sci.* 2024;262:108710.
doi: 10.1016/j.ijmecsci.2023.108710

39. Ni X, Sun Q, Wang J, et al. Development and characterization of minimal surface tantalum scaffold with high strength and superior fatigue resistance. *J Mater Res Technol*. 2025;36:1226-1239.
doi: 10.1016/j.jmrt.2025.03.108

40. Liu J, Zou Z, Li Z, et al. A clustering-based multiscale topology optimization framework for efficient design of porous composite structures. *Comput Methods Appl Mech Eng.* 2025;439:117881.
doi: 10.1016/j.cma.2025.117881

41. Noman AA, Shaari MS, Mehboob H, Azman AH. Recent advancements in additively manufactured hip implant design using topology optimization technique. *Results Eng.* 2025;25:103932.
doi: 10.1016/j.rineng.2025.103932

42. Kök HI, Kick M, Akbas O, et al. Reduction of stress-shielding and fatigue-resistant dental implant design through topology optimization and TPMS lattices. *J Mech Behav Biomed Mater.* 2025;165:106923.
doi: 10.1016/j.jmbbm.2025.106923

43. Xiong W, Ding X, Zhang H, et al. Topology optimization of embracing fixator considering bone remodeling to mitigate stress shielding effect. *Med Eng Phys.* 2024;125:104122.
doi: 10.1016/j.medengphy.2024.104122

44. Peng W, Cheng K, Liu Y, et al. Biomechanical and mechanostat analysis of a titanium layered porous implant for mandibular reconstruction: the effect of the topology optimization design. *Mater Sci Eng C-Mater Biol Appl.* 2021;124:112056.
doi: 10.1016/j.msec.2021.112056

45. Smit T, Aage N, Haschtmann D, Ferguson SJ, Helgason B. Anatomically and mechanically conforming patient-specific spinal fusion cages designed by full-scale topology optimization. *J Mech Behav Biomed Mater.* 2024; 159:106695.
doi: 10.1016/j.jmbbm.2024.106695

46. Gao H, Jin X, Yang J, et al. Porous structure and compressive failure mechanism of additively manufactured cubic-lattice tantalum scaffolds. *Mater Today Adv.* 2021;12:100183.
doi: 10.1016/j.mtadv.2021.100183

47. du Plessis A, Razavi SMJ, Benedetti M, et al. Properties and applications of additively manufactured metallic cellular materials: a review. *Prog Mater Sci.* 2022;125:100918.
doi: 10.1016/j.pmatsci.2021.100918

48. Wang J, Ni X, Sun Q, et al. Additively manufactured trabecular porous tantalum: effects of annealing temperature and oxygen content on mechanical properties. *J Mater Res Technol*. 2025;35:4055-4070.
doi: 10.1016/j.jmrt.2025.02.030

49. Qin F, Chen L, Zhou G, Shi Q, Liu B, Liu X. Improved compressive strength of laser powder bed fused porous tantalum by hot isostatic pressing. *Addit Manuf.* 2025;102:104729.
doi: 10.1016/j.addma.2025.104729

50. Liu L, Yi B, Wang T, Li Z, Zhang J, Yoon GH. Investigation on numerical analysis and mechanics experiments for topology optimization of functionally graded lattice structure. *Addit Manuf.* 2021;47:102275.
doi: 10.1016/j.addma.2021.102275

51. Ahmadi SM, Campoli G, Yavari SA, et al. Mechanical behavior of regular open-cell porous biomaterials made of diamond lattice unit cells. *J Mech Behav Biomed Mater.* 2014;34:106-115.
doi: 10.1016/j.jmbbm.2014.02.003

52. Gibson LJ, Ashby MF, eds. *Cellular Solids: Structure and Properties*. Cambridge: Cambridge University Press; 1999.

53. Zhang YT, Aiyiti W, Du S, Jia R, Jiang HF. Design and mechanical behaviours of a novel tantalum lattice structure fabricated by SLM. *Virtual Phys Prototyp.* 2023;18(1):e2192702.
doi: 10.1080/17452759.2023.2192702

54. Ataee A, Li Y, Fraser D, Song G, Wen C. Anisotropic Ti-6Al-4V gyroid scaffolds manufactured by electron beam melting (EBM) for bone implant applications. *Mater Des.* 2018;137:345-354.
doi: 10.1016/j.matdes.2017.10.040

55. Regassa Hunde B, Debebe Woldeyohannes A. Future prospects of computer-aided design (CAD) – a review from the perspective of artificial intelligence (AI), extended reality, and 3D printing. *Results Eng*. 2022;14:100478.
doi: 10.1016/j.rineng.2022.100478

56. Benady A, Meyer SJ, Golden E, Dadia S, Katarivas Levy G. Patient-specific Ti-6Al-4V lattice implants for critical-sized load-bearing bone defects reconstruction. *Mater Des.* 2023;226:111605.
doi: 10.1016/j.matdes.2023.111605

57. Moscol-Albañil I, Solórzano-Requejo W, Rodriguez C, Ojeda C, Díaz Lantada A. Innovative AI-driven design of patient-specific short femoral stems in primary hip arthroplasty. *Mater Des.* 2024;240:112868.
doi: 10.1016/j.matdes.2024.112868

58. Zhang T, Liu F, Chen J, et al. Dual-graded lattice with mechanical bionics to enhance fatigue performance. *Int J Mech Sci.* 2024;279:109474.
doi: 10.1016/j.ijmecsci.2024.109474

59. Wang B, Liu M, Ke W, Hua W, Zeng X, Yang C. Finite element analysis of additive manufactured porous peek artificial vertebral bodies in lumbar total en bloc spondylectomy. *Spine J*. 2025;25(5):1042-1049.
doi: 10.1016/j.spinee.2024.10.026

60. Zhang H, Guo Z, Zhang Z, Wu G, Sang L. Biomimetic design and fabrication of PEEK and PEEK/CF cage with minimal surface structures by fused filament fabrication. *J Mater Res Technol.* 2023;26:5001-5015.
doi: 10.1016/j.jmrt.2023.08.236

61. Hu B, Wang L, Song Y, et al. A comparison of long-term outcomes of nanohydroxyapatite/polyamide-66 cage and titanium mesh cage in anterior cervical corpectomy and fusion: a clinical follow-up study of least 8 years. *Clin Neurol Neurosurg.* 2019;176:25-29.
doi: 10.1016/j.clineuro.2018.11.015

62. Chen Y, Chen D, Guo Y, et al. Subsidence of titanium mesh cage: a study based on 300 cases. *Clin Spine Surg.* 2008;21(7):489-492.
doi: 10.1097/BSD.0b013e318158de22

63. Lostado Lorza R, Somovilla Gomez F, Corral Bobadilla M, et al. Comparative analysis of healthy and cam-type femoroacetabular impingement (FAI) human hip joints using the finite element method. *Appl Sci-Basel.* 2021;11(23).
doi: 10.3390/app112311101

64. McCartney W, MacDonald B, Ober CA, Lostado-Lorza R, Gómez FS. Pelvic modelling and the comparison between plate position for double pelvic osteotomy using artificial cancellous bone and finite element analysis. *BMC Vet Res.* 2018;14(1):100.
doi: 10.1186/s12917-018-1416-1

65. Gómez FS, Lorza RL, Bobadilla MC, García RE. Improving the process of adjusting the parameters of finite element

models of healthy human intervertebral discs by the multi-response surface method. *Materials*. 2017;10(10). doi: 10.3390/ma10101116

66. Íñiguez-Macedo S, Somovilla-Gómez F, Lostado-Lorza R, Corral-Bobadilla M, Martínez-Calvo MÁ, Sanz-Adán F. The process of designing a rotating platform artificial knee prosthesis with posterior stabilizers by finite element analysis. *Int J Interact Des Manuf.* 2018;12(3):853-864. doi: 10.1007/s12008-017-0428-6

67. Somovilla-Gómez F, Lostado-Lorza R, Corral-Bobadilla M, Escribano-García R. Improvement in determining the risk of damage to the human lumbar functional spinal unit considering age, height, weight and sex using a combination of FEM and RSM. *Biomech Model Mechanobiol.* 2020;19(1):351-387. doi: 10.1007/s10237-019-01215-4